applied sciences

MDPI

Article

A Robust Adiabatic Model for a Quasi-Steady Prediction of Far-Off Non-Measured Performance in Vaneless Twin-Entry or Dual-Volute Radial Turbines

José Ramón Serrano *,†, Francisco J. Arnau †, Luis Miguel García-Cuevas † and Vishnu Samala †

CMT-Motores Térmicos, Universitat Politècnica de València, Camino de Vera s/n, 46022 València, Spain; farnau@mot.upv.es (F.J.A.); luiga12@mot.upv.es (L.M.G.-C.); vissa@posgrado.upv.es (V.S.)

* Correspondence: jrserran@mot.upv.es (J.R.S.); Tel.: +34-963879657; Fax: +34-963877659

† These authors contributed equally to this work.

Received: 31 January 2020; Accepted: 9 March 2020; Published: 12 March 2020

Abstract: The current investigation describes in detail a mass flow oriented model for extrapolation of reduced mass flow and adiabatic efficiency of double entry radial inflow turbines under any unequal and partial flow admission conditions. The model is based on a novel approach, which proposes assimilating double entry turbines to two variable geometry turbines (VGTs) using the mass flow ratio (*MFR*) between the two entries as the discriminating parameter. With such an innovative approach, the model can extrapolate performance parameters to non-measured *MFR*s, blade-to-jet speed ratios, and reduced speeds. Therefore, the model can be used in a quasi-steady method for predicting double entry turbines performance instantaneously. The model was validated against a dataset from two different double entry turbine types: a twin-entry symmetrical turbine and a dual-volute asymmetrical turbine. Both were tested under steady flow conditions. The proposed model showed accurate results and a coherent set of fitting parameters with physical meaning, as discussed in this paper. The obtained parameters showed very similar figures for the aforementioned turbine types, which allows concluding that they are an adequate set of values for initializing the fitting procedure of any type of double entry radial turbine.

Keywords: turbocharger; twin-entry radial turbines; dual-volute radial turbines; unequal and partial flow admission; quasi-steady models; adiabatic efficiency model; reduced mass flow model.

1. Introduction

Along with the growing interest in global environmental issues, the automotive manufacturers are facing increasing challenges to reduce the gaseous emissions [1] coming from internal combustion engines as well as to meet the strict emission legislation year by year [2]. Despite the rapid growth of electric car sales in recent years, internal combustion engines will continue to be active until at least 2050, according to recent studies [3]. Moreover, nowadays, battery electric vehicles have heavy CO_2 footprints when analyzed from cradle to grave [4,5]. It is foreseen that plug-in hybrid powertrains, and small capacity turbocharged engines will cover the major part of passenger cars needs in decades ahead [6]. To compete with an electric powertrain, automotive engineers are developing new internal combustion engines to be environmentally friendly, while keeping the vehicle performance and having sufficiently attractive fuel consumption to satisfy the customers' requirements. Over the years, automotive OEMs are increasingly downsizing their engines, which has been demonstrated to be an efficient way in reducing the engine CO_2 emissions with promising cost-to-benefit ratios compared with many other advanced ICE technologies [7]. To assure the same engine brake output power and

performance with the reduction in cylinder displacement, downsizing technologies need to use forced induction-turbocharging. The traditional single entry turbine is widely used in turbochargers, due to its straightforward construction. This has given many advantages in terms of fuel consumption and emissions reductions with the previous and current regulations. However, concerning the future legal requirements for low emissions (Euro 6d Full and Euro 7 regulations) with fuel efficiency, there is still need and potential for optimization.

Nevertheless, a turbocharger turbine always confronts high unsteadiness of flows coming from the reciprocating internal combustion engine [8]. In recent years, automotive OEMs are seeing much interest in using the double entry turbines, especially for four cylinders turbocharged petrol engines with wide valves overlap period in their timing diagram or in six-cylinder compression ignition engines [9]. They have the advantages of utilizing the pulse energy coming from the engine exhaust and minimizing the interferences between the cylinders during the exhaust process (engine pumping losses). Some engine manufacturers choose twin-entry turbines (where the turbine scroll is meridionally divided, as shown in Figure 1a); others opt for the dual-volute turbine (turbine scroll is circumferentially divided, as shown in Figure 1b). The comparison of performance parameters between these two types of double entry turbines has been extensively discussed since Pischinger and Wunsche [10] until more recently, such as in the work by Romagnoli et al. [11].

Moreover, both turbines (twin-entry/dual-volute) have different geometries due to their designs, merely by the type of flow division, as explained below:

- Twin-entry turbine (T#1TE): The scroll has a single wall around the entire perimeter of the turbine housing such that each entry admits the exhaust gas over the whole circumference of the turbine wheel. The entry closer to the turbine outlet is named as Shroud (Sh), and the entry which is closer to the bearing housing side is called as Hub (H), and the same is shown in Figure 1a.
- Dual-volute turbine (T#2DV): The scroll is divided in a way that each scroll admits the exhaust gas at a separate section of the rotor. The turbine scroll which has a longer volute is named as Long Volute (LV), and the scroll which has a shorter volute is named as Short Volute (SV), as shown in Figure 1b.

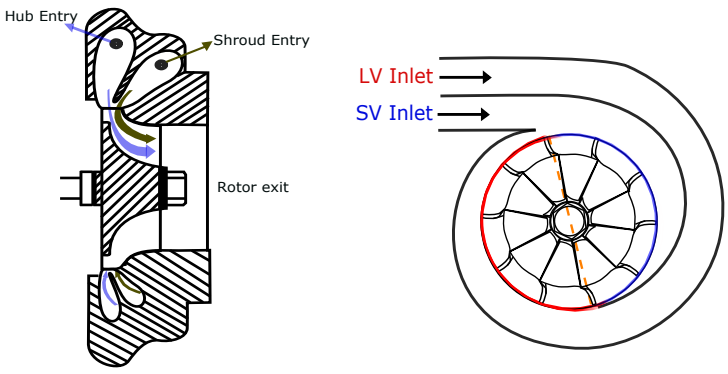

Figure 1. Difference in double entry radial turbine geometries due to their designs. (**a**) Twin-entry turbine (T#1TE) [12], (**b**) Dual-volute turbine (T#2DV).

Hereafter, the respective turbocharger turbine entries/scroll are referred to by their names.

It is worth highlighting that the flow conditions between the entries of a double entry radial inflow turbine can be divided into three different categories as follows:

- Full/equal admission have the same mass flow rate in each entry of the turbine.
- Unequal admission have different inlet temperature, pressure, and mass flow levels between the entries of a double entry radial inflow turbine.

- Partial admission block one of the turbine inlets and pass the flow through the open channel and vice versa.

In normal engine operation conditions, the twin-entry or dual-volute turbochargers operate under different flow admission conditions due to the pulsating exhaust gas natures coming from the engine. However, it should be noted that the partial admission condition is not possible to appear continuously under regular engine operating conditions. Many researchers have also reported that the engine exhaust pulsatile flows significantly influence the performance of a double entry turbine powered turbocharger [13–15]. Even though partial admission is not often found in automotive applications, it is a quite important operation regime in other energy conversion and management processes. These kinds of radial turbines are used for obtaining electric power from renewable energy sources, such as geothermal energy [16,17], solar energy [18], and compressed air energy storage systems [19]. The Organic Rankine Cycle (ORC) is widely used for these types of energy conversions with an appropriate working fluid because it converts low-grade thermal energy into useful energy [20]. In ORCs, the available thermal energy as a renewable heat source is not supplied continuously due to the variations of available thermal energy [21–23]. In this case, the regulation of radial inflow turbines based on partial admission operations is standard practice. The model proposed in this work would also help to better simulate such essential regulation maneuvers in radial turbines.

Nowadays, automotive manufacturers are focusing on a wide range of engine operating conditions which are different from traditional full load operation. To achieve an optimum matching between the turbocharger and internal combustion engines, automotive manufacturers are relying on one-dimensional engine cycle simulation tools to predict and study the effect of various parameters on engine performance. 1D simulation codes make possible the calculation of gas dynamics engine behavior at low computational costs. Furthermore, the method also shows a critical approach to simulate the unsteady performance of the turbine [24]. Moreover, the exhaust system is essential for meeting the emissions limits across the operating range of the engine. As asserted in [13], during the engine part loads and transient conditions for the internal combustion engines, the turbocharger turbine works at off-design conditions. It is not viable to capture this behavior by the standard turbine maps provided by the manufacturers, as they only offer a narrow range of data that they could measure in the gas stand. Therefore, the turbocharger turbine models should be capable of simulating the real-life conditions, so that the prediction of exhaust gas mass flow, the pressure drop across the turbine and the energy transfer to the compressor is essential.

Turbine map extrapolation tools are necessary when using one-dimensional modeling tools to predict the system's behavior outside of the turbine design operative conditions [25]. Numerous researchers were able to succeed in modeling the extrapolation tools for conventional single entry fixed and variable geometry turbines [26–30]. Some of these models are more physical and are able to calculate the losses generated in the turbine while extrapolating the efficiency maps to off-design conditions [31].

Mainly, turbocharger turbine models are based on steady flow maps. By providing information about the mass flow rate and isentropic efficiency, they solve the system of equations by assuming a quasi-steady behavior. In the case of double entry turbines, the steady flow map under full admission condition (where the flow is the same in both entries of the turbine) is not enough for simulation purposes. In reality, the exhaust pulses feeding each entry of the turbine will be timed so that they are out of phase with each other; as a result, double entry turbines spend little time in full admission and the majority of the time with unequal flows in their entries. Therefore, the turbine maps should also cover the necessary flow conditions such as unequal and partial admissions between their entries [22]. Moreover, the addition of the second inlet to the turbine volute brings extra complexity in determining the steady-state turbine performance parameters. Addressing this, in previous work [12], a detailed analysis of experimental data and how to process the performance parameters of twin-entry radial-inflow turbine was shown for different steady flow admission conditions. Furthermore, an

overview of the previous work is presented in this paper and the same techniques were applied to process the experimental data of a dual-volute turbocharger.

Many methods for mean-line modeling of twin-entry turbines are available in the literature. However, at partial and unequal admission conditions, the prediction of efficiency from the models seem to be very difficult to obtain [32]. Hajilouy Benisi et al. [33] developed a twin-entry turbine model by modifying the one-dimensional equations, which are used to analyze the flow in single entry turbine. In addition, the loss models of single entry turbines were applied to the twin-entry by making some changes. By doing this, some predicting results were obtained. However, the authors pointed out that the calculated efficiency and the mass flow are overestimated. In the case of partial admission conditions, there was a remarkable difference between predicted and experimental data. Costall et al. [34] developed a model for twin-entry turbines and solved it using a gas dynamics code. The pulse flow performance of a twin-entry turbine under unequal and full admission conditions was analyzed, suggesting that, for full admission flow states, twin-entry turbine can be modeled as a simplified single entry model, whereas for unequal flows a more complex model is necessary.

Moreover, the complete unequal admission maps are not always available because many gas stands are not capable of operating in those conditions. Addressing this, Romagnoli et al. [11] proposed a map-based method for predicting the partial and unequal admission flows in double entry turbines (both twin and dual) from a given full admission map. Based on the experimental data, two correlations were proposed, one for twin-entry and another for a dual-volute turbine, and they concluded that the twin-entry turbine characteristic agreed reasonably well with their approach. However, the correlation with the performance of a dual-volute turbine was less satisfactory. Newton et al. [35] proposed a method for extrapolating from the full admission map of the dual-volute turbine to obtain the unequal admission performances of both efficiency and mass flow parameters. The model is dependent on three constants: one of them is used for predicting the efficiency ratio between the unequal and full admission data points and the other two are used for estimating the mass flow ratio parameter. The values of the constants are determined by using the minimal amount of unequal admission flow data at different turbine speeds. The study concluded with good agreement between the model predictions and experimental results. However, the analysis was restricted to one dual-volute geometry turbine and it is not sure whether the same results can be found for another similar turbocharger without further experimental campaigns. Moreover, the model also requires a significant amount of experimental data for finding the values of the fitting constants. Chiong et al. [36] studied the pulse flow modeling of a twin-scroll turbine under pulse flow operating conditions and pointed out that the overall performance prediction of the model can be enhanced by taking into account the partial admission characteristics during modeling.

Fredriksson et al. [37] proposed a mean-line model for asymmetrical twin-entry turbine by specifying different flow conditions at each turbine inlet and static pressure at the outlet of a turbine. The methodology is to solve each turbine passage from inlet to the splitter location separately, and from the volute splitter to the rotor inlet, two streams mix into one uniform flow. The model further considers the swirl energy loss from the divider wall to the rotor inlet in the form of pressure loss. The results demonstrate that the mass flow parameters are well predicted for full and partial admission flow conditions and efficiencies were over-predicted in the case of lower turbo speeds and pressure ratios. Macek et al. [38] proposed a more complex model for twin-entry turbine using a loss parameters calibration criteria and the modeling was based on approximation of real physics. Palenschat et al. [39] implemented three significant changes in the single-entry model of Romagnoli and Martinez-Botas [27] for predicting the variables of asymmetrical twin-entry turbine. Firstly, they added the second entry model having the calculation procedure being identical to that of the single entry model. Secondly, they added inlet duct models each one of the entries to resemble the flow passage from the turbine inlet to the tongue. Third, they included the interspace model to obtain the resulting flow angle and the flow properties after the mixing. The model was validated with three flow conditions: equal pressure, equal mass flow, and unequal flow admissions. It was concluded that the performance of the model is best

at equal-pressure conditions and becomes worse as flow imbalance between the branches is increasing. The root mean square analysis showed that the model was able to predict all the parameters within 10% error concerning the experimental data for similar pressure conditions and, in unequal admission flows, the difference in mass flow parameter between the model and experimental was about 20%.

The current paper demonstrates the methodology for modeling both twin-entry and dual-volute turbines to extrapolate the performance maps into off-design conditions for all the flow admission conditions. The approach for modeling this is the same for both types of turbines, and it is mainly based on systematizing the characteristic maps of the turbine, which is explained in [12]. The paper is divided into five main sections. In Section 2, an experimental method to obtain the performance maps of a double entry turbine at different mass flow ratios is summarized. In Sections 3 and 4, the VGT model of Serrano et al. [30] (which is summarized in Appendix A) is re-designed and adapted to work for double entry turbines. The re-design procedure is done using data from one of the two types of double entry turbines analyzed in this work (twin-entry). The results of modeling are discussed by comparing with the experimental data for both types of double entry turbines (twin-entry and dual-volute). The main variables are reduced mass flow and apparent adiabatic efficiency. This apparent efficiency is a magnitude proposed and defined in this paper to achieve the proposed objectives. In Section 5, a new model for double entry turbines efficiency fitting and calculation is detailed with a procedure based on a merit function pointing to the defined apparent efficiency to predict the behavior of every turbine branch under all the tested *MFR* and BSR conditions. The proposed model is further validated with a different type of double entry radial-inflow turbine, namely a dual-volute asymmetric radial-inflow turbine. In Section 6, the procedure for extrapolating the turbine maps of double entry turbine is discussed. In Section 7, conclusions of the work are presented.

2. Experimental Study

To develop the flow oriented model as well as extrapolate and interpolate the maps, the twin-entry and dual-volutes turbine measurements are needed. A turbocharger test rig has been designed to investigate this type of turbochargers under a variety of operational conditions, based on the flow simulation of a turbocharger using compressed air [12].

Figure 2 shows the schematic representation of the test rig and its main components. The test rig is fed by a two-stage, oil-free centrifugal compressor, which is the oil-free type and powered by a 450 kW electric motor. The flow capacity ranges 4000–7200 Nm^3/h and a maximum relative pressure of 5.30 bar can be reached. The combustion chamber shown in Figure 2 is not operated as the tests were performed in quasi-adiabatic conditions with a turbine inlet temperature around 363 K. Downstream of the combustion chamber, the airflow is branched into two pipes, which are called Turbine Entry 1 (for Sh/LV) and Turbine Entry 2 (for H/SV), referring to their positions shown in Figure 3. Each of these branches is instrumented with a V-cone type sensor for measuring the air mass flow rate and a control valve for varying the flow going into the branch, allowing to test the turbocharger with different flow admission conditions. At the downstream of the turbine, a third V-cone sensor is placed for measuring the total mass flow exiting from the turbine. There is also a possibility of changing the outlet conditions of the turbocharger compressor using back-pressure valves. The objective was to obtain the adiabatic efficiency maps of the turbine at different flow admission conditions. The ducts and turbochargers are thermally insulated, as shown in Figure 4b, to reduce the extern al heat transfer. Sensors to measure the parameters such as pressure, temperature, turbocharger speed, and mass flow rate at the essential sections of the various fluids are also available and their measurement precisions are shown in Table 1.

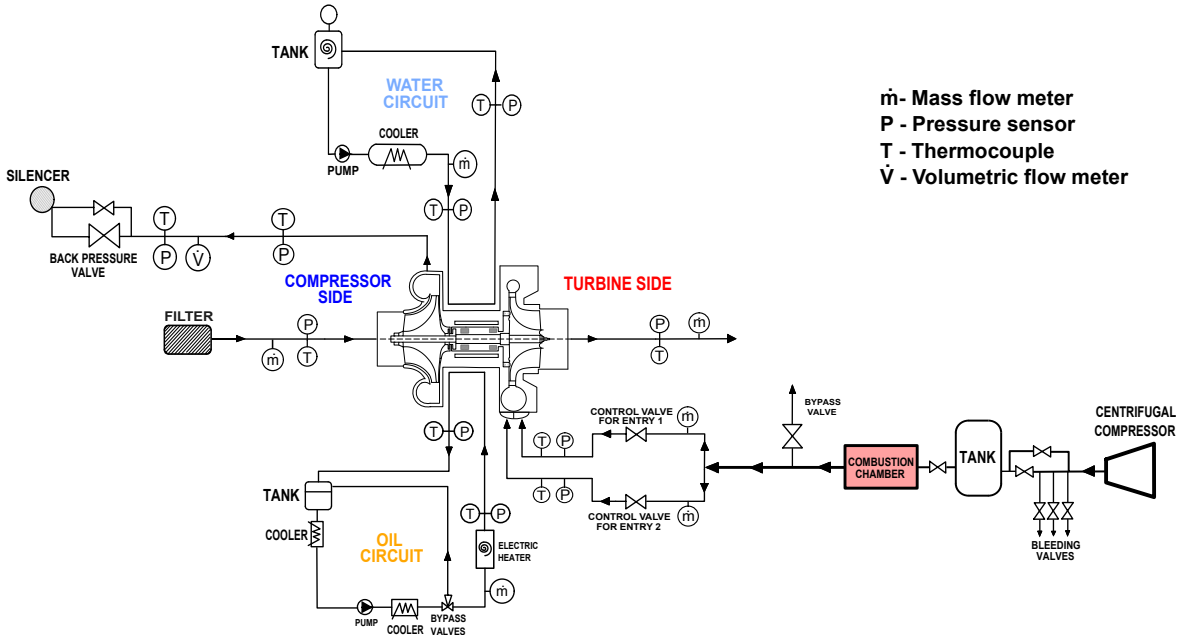

Figure 2. Schematic layout of a turbocharger gas stand for testing the double entry turbine. The locations of the main sensors are also shown.

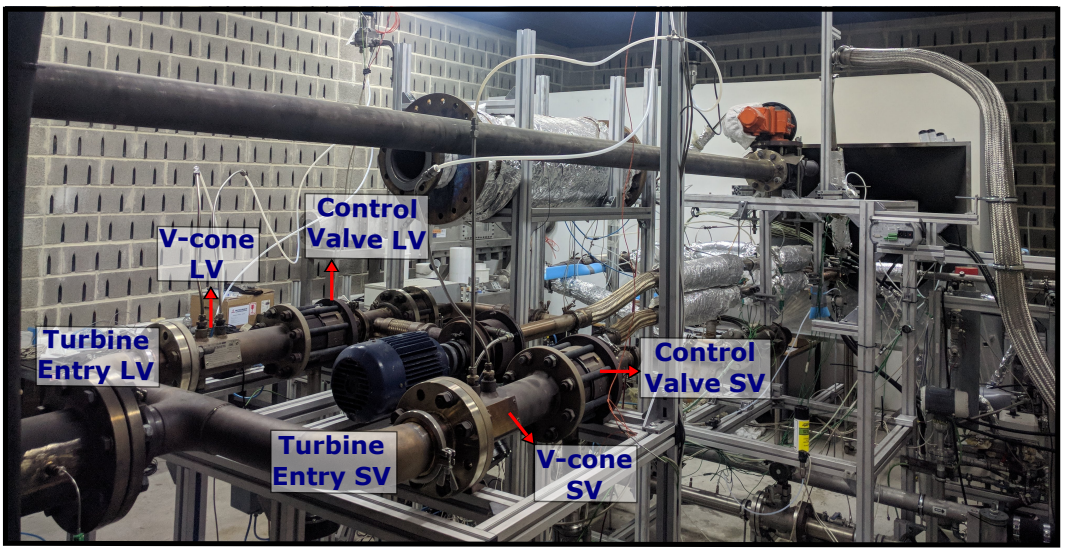

Figure 3. Gas stand for testing the double entry turbines at different flow admission conditions in steady flow situations.

Table 1. List of main sensors used in the experimental work , showing their typical uncertainty.

Variable	Sensor Type	Range	Typical Uncertainty
Gas mass flow	V-cone and Thermal vortex	45–1230 kg/h	<1% of the measured values
Gas pressure	Piezoelectric	0 to 5 bar	12.5 mbar
Gas/metal temperature	K-type thermocouple	273 K to 1500 K	1.5 K
Oil pressure	Piezoelectric	0 to 5 bar	12.5 mbar
Oil temperature	RTD	173 K to 723 K	<0.5 K
Oil mass flow	Coriolis	Few tens gr/s	2 % of the measured value
Turbocharger speed	Inductive sensor	<300 krpm	<500 rpm

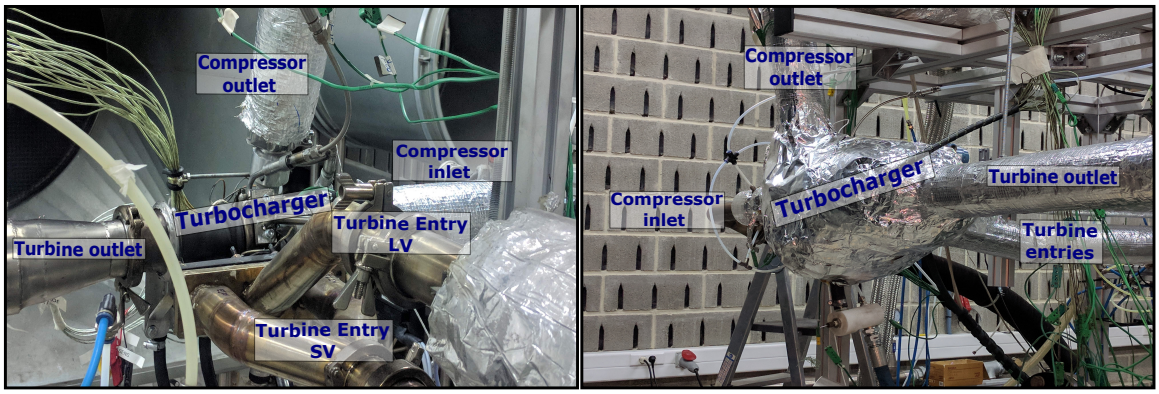

(**a**) Turbocharger in the gas stand before insulation (**b**) Turbocharger in the gas stand after insulation

Figure 4. Dual-volute turbocharger setup in the gas stand.

Finally, the turbochargers were tested in partial, full, and unequal admission conditions for modeling purpose. It is worth highlighting that the unequal admission was tested by feeding each entry with an unequal amount of steady flow in steady state conditions. The different admission tests are defined according to the mass flow ratio definition [12] as shown in Equation (1), where the actual mass flow rate in shroud/long volute entry has been divided by the overall mass flow rate through the turbine.

$$MFR = \frac{\dot{m}_{Sh/LV}}{\dot{m}_{Sh/LV} + \dot{m}_{H/SV}} \quad (1)$$

The main points of the turbocharger test facility and the methodology for testing the twin-entry or dual-volute turbine in a quasi-adiabatic state were demonstrated with the measurement uncertainty in earlier work [12]. The experimental data presented in [12] have been used here for the correlation of the model. Similar testing conditions were used for examining the dual-volute turbocharger, and the data were used for the model validation.

Performance Parameters

The experiments provided the necessary data to calculate turbine map parameters: reduced mass flow, reduced turbine speed, expansion ratio, adiabatic efficiency, and blade to jet speed ratio. As described by Serrano et al. [12], representing the double entry turbine performance parameters with the average values between the two entries (e.g., expansion ratio and turbine scroll temperature) showed an impact on resulting maps and made it difficult to analyze the parameters. Moreover, representing both branches with one turbine flow parameter, the mass flow distribution between respective entries under equal and unequal admission conditions is not known. Thus, as detailed in [12], the two entries are treated separately for calculating the turbine map parameters as follows.

In the following equations, the term i represents the generic code for the turbine inlet branch. The reduced turbine speed n_{red} is computed for each branch using appropriate turbine scroll inlet temperature, as shown Equation (2).

$$n_{red,i} = \frac{n}{\sqrt{T_{0t,i}}} \quad (2)$$

where n is the turbocharger speed and $T_{0t,i}$ is the turbine total inlet temperature at the corresponding turbine entry. The turbine reduced mass flow rate $\dot{m}_{\text{red}}$ is computed for each entry, as shown in Equation (3)

$$\dot{m}_{red,i} = \frac{\dot{m}_i \cdot \sqrt{T_{0t,i}}}{p_{0t,i}} \quad (3)$$

where $\dot{m}_i$ and $p_{0t,i}$ are the turbine mass flow rate and total inlet pressure for a corresponding entry. The turbine total to static pressure ratio $\Pi_{i(0t,4)}$ is estimated by Equation (4). p_4 is the common turbine outlet pressure and therefore it does not have an index.

$$\Pi_{i,(0t,4)} = \frac{p_{0t,i}}{p_4} \tag{4}$$

When the twin-entry/dual-volute turbine is working in an engine, the inlet conditions are changed in both branches due to the staggered firing orders in the cylinders [40] and corresponding interval opening of the cylinders valves [41]. Accordingly, it was assumed that the power produced by each turbine branch is different [12]. Therefore, the turbine total to static efficiency was computed as two individual turbines, as shown in Equation (5), on the basis of the enthalpy–entropy adiabatic expansion of the turbine shown in Figure 5. Hereafter, it is referred as apparent efficiency.

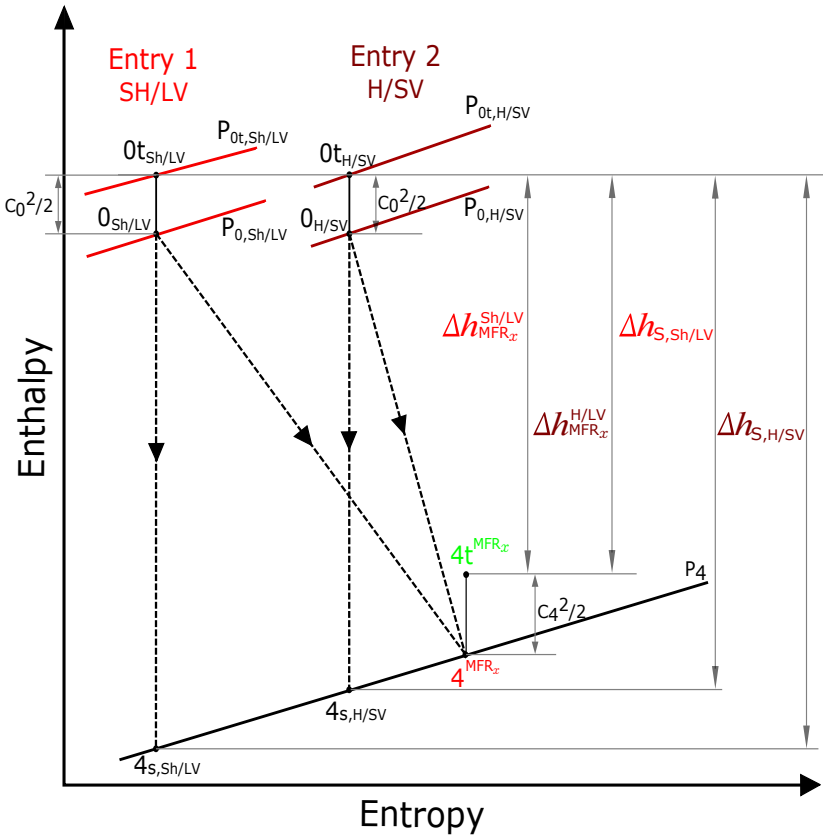

Figure 5. Enthalpy–entropy expansion process in twin-entry/dual-volute radial turbines.

$$\eta^{i}_{MFR_x(t/s)} = \frac{T_{0t,i} - T^{MFR_x}_{4t}}{T_{0t,i} - T_{4s,i}} \tag{5}$$

where $T^{MFR_x}_{4t}$ is the mass averaged mixed turbine outlet total temperature that is measured in the gas stand. Since the temperature that is coming from the individual turbine branches is mixed at the turbine outlet station (see Figure 5), it is a convenient method to assume the outlet stations are at equal temperatures [12]. $T_{4s,i}$ is the isentropic turbine temperature and it is estimated independently for both turbine entries as shown in Equation (6).

$$T_{4s,i} = T_{0t,i} \cdot \left(\frac{1}{\Pi_{i,(0t,4)}} \right)^{\frac{\gamma-1}{\gamma}} \tag{6}$$

Lastly, Equation (7), shows the definition of a blade to jet speed ratio, which is estimated for each branch with their corresponding inlet temperature and expansion ratio.

$$\sigma_i = \frac{2 \cdot \pi \cdot n \cdot r_3}{\sqrt{2 \cdot c_p \cdot T_{i,0t} \cdot \left[1 - \left(\frac{1}{\Pi_{i,(0t,4)}}\right)^{\frac{\gamma-1}{\gamma}}\right]}} \tag{7}$$

By treating both turbine inlet branches separately, it is possible to obtain two different efficiency maps linked to the mass flow parameter maps, as shown in Figure 6 (here, the experimental results of dual-volute turbocharger are shown, since the followed procedure is the same as for the twin-entry turbine that was determined in [12]). The mass flow parameter and efficiency data are normalized by the experimental maximum values of every scroll.

It can be observed in Figure 6a,c that the flow parameter maps show comparable characteristics to any single-entry variable geometry turbine (VGT) [42]. The non-linear relation between *MFR* and reduced mass flow is also noticeable. For instance, in the case of long volute (Figure 6a), there are small differences between reduced mass flow values at *MFR* = 1 and *MFR* = 0.65 and a much higher difference among *MFR* = 0, *MFR* = 0.22, and *MFR* = 0.5. The same phenomenon is observed in the short volute case (Figure 6c) but with the opposite trend, i.e., the high difference among *MFR* = 1, *MFR* = 0.65, and =0.5 and almost the same values for *MFR* = 0.22 and *MFR* = 0. Furthermore, Figure 6b,d shows that there are significant differences in apparent efficiencies between Long Volute (LV) and Short Volute (SV). As mentioned in [12], the apparent efficiency is useful to introduce order for the characterization of double entry turbines such as twin-entry/dual-volute. However, it is not a good efficiency definition, for the case of unequal admission, to reflect which branch is extracting energy more efficiently from the flow upstream the turbine. It is, however, in the cases of *MFR* = 0 and *MFR* = 1 for partial admissions and *MFR* = 0.5, at which the turbine is acting as full admission and has almost the same mass flow in both branches, where the apparent efficiency interpretation signifies the energy extraction of every branch reasonably.

The performance maps obtained using the method proposed in [12] provided reliable information of flows going into each turbine branch at different flow admission states. In addition, this approach allows using the current VGT turbine models as two turbines and extrapolating the mass flow and efficiency parameters to off-design conditions.

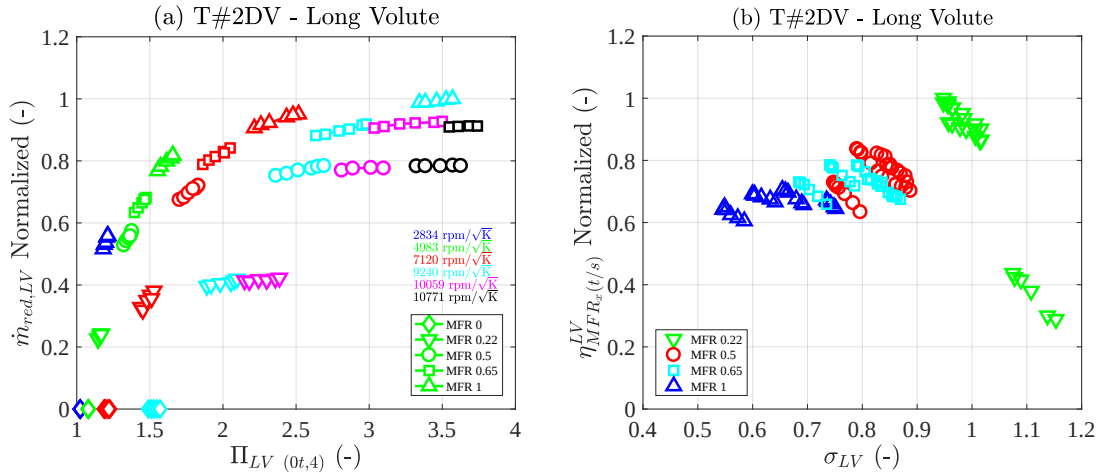

Figure 6. *Cont.*

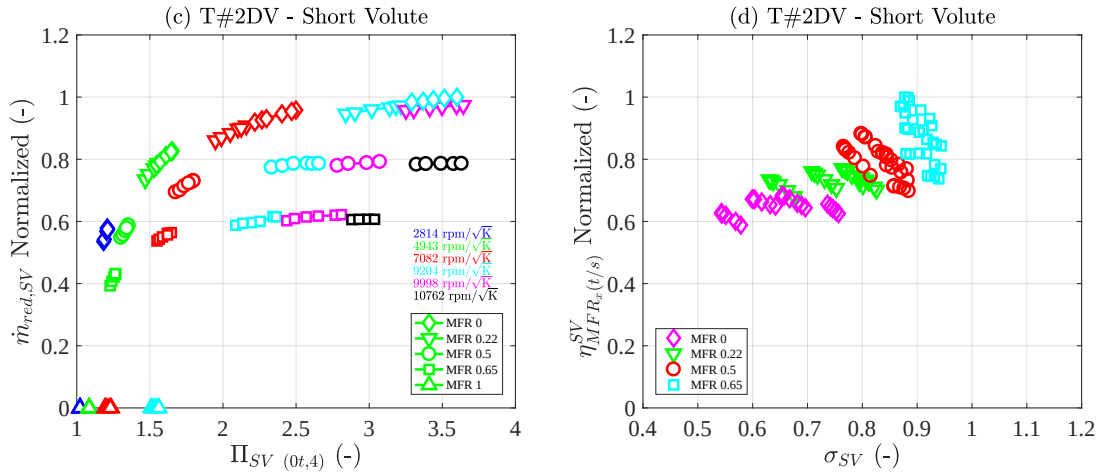

Figure 6. Turbine flow and efficiency maps of a dual-volute turbocharger (T#2DV).

3. Reduced Mass Flow Fitting

The approach of considering the two entries as individual turbines makes the resulting mass flow parameters show an explicit dependency of the flow behavior with the mass flow ratio (*MFR*, Equation (1)) (referring to Figure 6 and [12]). Accordingly, the model presented by Serrano et al. [30], which is briefly described in Appendix A.1, is re-designed to deal with twin-entry and dual-volute turbines.

The model considers now two turbine entries as two separate equivalent nozzles, as shown in Figure 7, each as if it were a VGT. These turbine entries have their respective set of maps depending on the *MFR* instead of the VGT position. The flow passage is divided into several regions, as shown in Figure 7 (station numbers are kept similar to the VGT turbine shown in Figure A1). The value of the effective area of two nozzles is calculated in the same way as in the case of a single entry VGT turbine, which uses the individual characteristic curves of expansion ratio versus reduced mass flow rate shown in Figure 6 for each branch.

Considering the assumption of two individual turbines, it is now possible to express the effective equivalent nozzle area for each entry, as shown in Equation (8).

$$A^j_{eff,i} = \frac{a^j_i \cdot A^{j\ geom}_{4,i} \cdot \sqrt{1 + \frac{\left(\sigma^j_i\right)^2 \cdot \left[\left(\frac{D^j_{4m,i}}{D^j_3}\right)^2 - 1\right]}{\overline{\eta}^i_{MFR_x(t/s)}} + b^j_i}}{\sqrt{1 + \left(c^j_i \cdot \frac{A^{j\ geom}_{4,i}}{A^{j\ geom}_{3,i}}\right)^2 \cdot \frac{\left(\frac{1}{\Pi^j_{i,(3,4)}}\right)^2}{\left[1 - \eta^i_{MFR_x(t/s)} \cdot \left(1 - \left(\frac{1}{\Pi^j_{i,(3,4)}}\right)^{\frac{\gamma-1}{\gamma}}\right)\right]^2}}} \tag{8}$$

$\Pi^j_{i,(3,4)}$ represents the pressure in the space between stator and rotor, estimated using Equation (9) with d^j_i as a fitting constant [30].

$$\Pi^j_{i,(3,4)} = 1 + d^j_i \cdot \left(\Pi^j_{i,(0t,4)} - 1\right) \tag{9}$$

In Equation (8), the terms i and j represent the generic codes for the turbine inlet (shroud or hub; long volute or short volute) and the turbocharger (twin-entry/dual-volute), respectively. Therefore, for each turbine, there are two effective area equations (one for each turbine entry), dependent on their

corresponding turbine entry geometries, the measured data of apparent efficiency ($\eta^{i}_{MFR_x(t/s)}$), and the four fitting constants (a^j_i, b^j_i, c^j_i, and d^j_i).

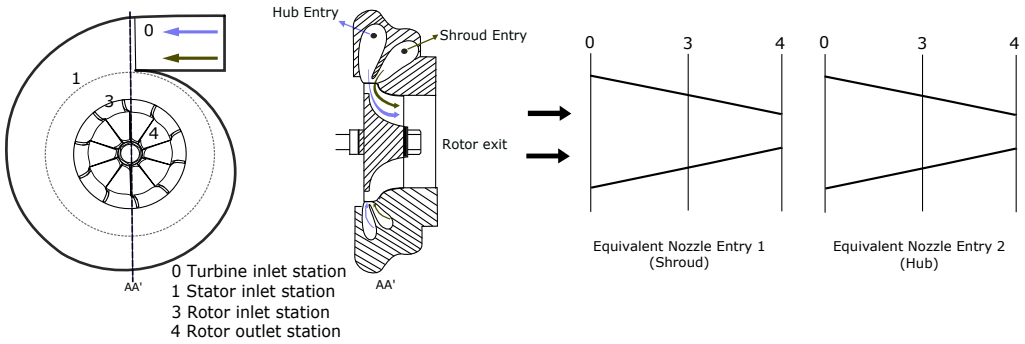

(**a**) The vaneless twin-entry radial turbine stations distribution and simplifying two entries into two equivalent nozzles

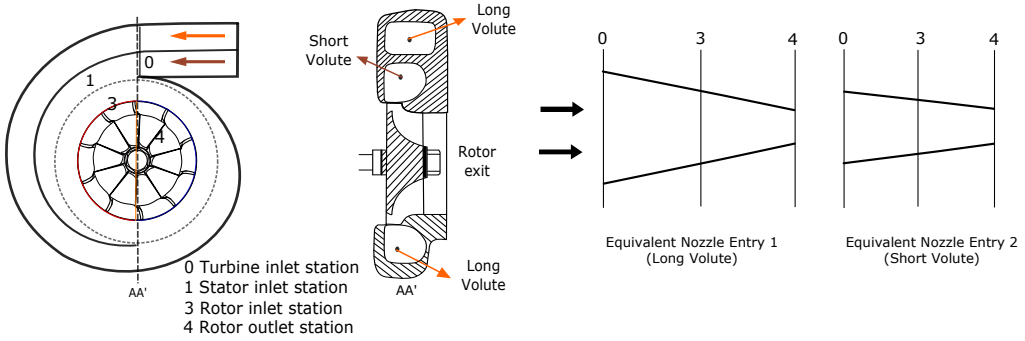

(**b**) The vaneless dual-volute radial turbine stations distribution and simplifying two volutes into two equivalent nozzles

Figure 7. Vaneless double entry turbines station distribution and modeling approach.

The effective area of the nozzle shown in Equation (8) is dependent on the stator and rotor outlet geometrical area. In the case of variable geometry turbine, these areas are estimated based on the geometry of the turbine and VGT positions, as outlined in Appendix A.1 and [30]. Nevertheless, twin-entry and dual-volute turbocharger used in this work are vaneless turbines. Therefore, the stator nozzle area is estimated using the turbine rotor diameter (D_3) and blade height (Bh), as shown in Equation (10) (see Figure 8). In vaneless turbines, it is considered that the stator outlet area is the same as the rotor inlet area.

$$A_3^{\text{geom}} = \pi \cdot D_3 \cdot Bh \tag{10}$$

For estimating the geometrical area at the rotor outlet, Equation (A4) can be used. In Equation (8), D_{4m} is an arithmetic mean diameter between turbine rotor shroud (D_4) and rotor hub (D_{nut}) diameters, as shown in Equation (11) (see Figure 8).

$$D_{4m} = \left(\frac{D_4 + D_{nut}}{2}\right) \tag{11}$$

As aforementioned, twin-entry and dual-volute turbines have different volute designs and geometries. Subsequently, the stator and rotor geometrical areas are estimated in different ways for every turbine type, as further explained below. To have a clear explanation, firstly the method for determining the geometrical areas of twin-entry turbine is defined, and then for a dual-volute turbine.

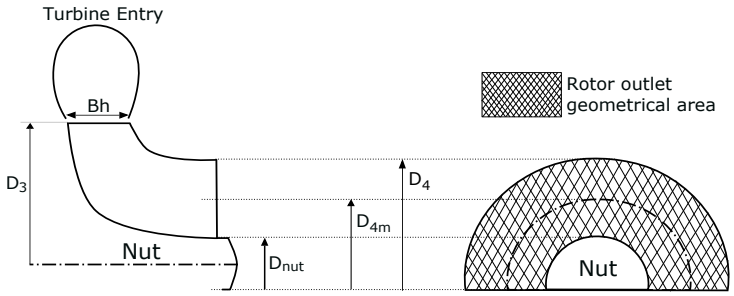

Figure 8. Geometrical description of vaneless turbine.

3.1. Twin-Entry Turbine

In twin-entry turbines, the induction flow path from the turbine inlet to the leading edge of the rotor blades is divided into shroud and hub branch, as shown in Figure 9. Due to the assumption of two individual turbines, the blade height has been shared between two branches by splitting the actual value in half (as in the current case it is symmetrical turbine). Subsequently, the stator area variation for two branches can be obtained as shown in Equation (12). In the case of asymmetric inlets, the proper fraction of blade height would be assigned for each turbine inlet.

$$A_{3,i}^{TE\ geom} = \pi \cdot D_3^{TE} \cdot \left(\frac{Bh^{TE}}{2} \right) \tag{12}$$

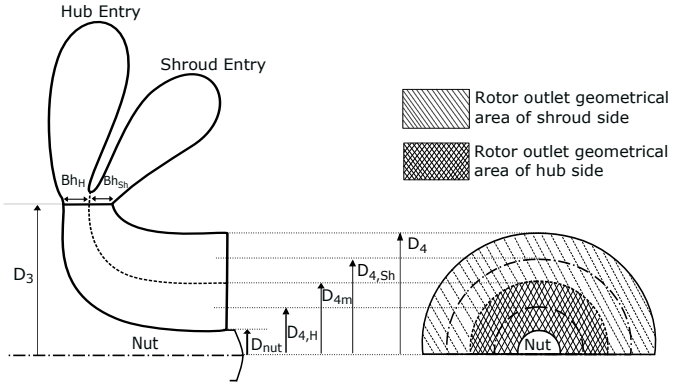

Figure 9. Geometrical description of twin-entry turbine (T#1TE).

For calculating the rotor outlet geometrical area ($A_{4,i}^{TE\ geom}$) in the case of twin-entry turbines, it is more relevant to consider the rotor outlet area for each branch in the view of two turbine approach modeling. For this purpose, the area estimated using Equation (A4) is shared equally between shroud and hub branch, as shown in Equation (13). By this, it is ensured that the mean-line (D_{4m}) divides the blade-to-blade duct into shroud and hub branches, as shown in Figure 9. Once the geometrical area of each branch is known, it is possible to estimate the rotor outlet mean diameters of shroud ($D_{4m,Sh}$) and hub ($D_{4m,H}$) branch using Equations (14) and (15) based on Figure 9

$$A_{4,i}^{TE\ geom} = \frac{A_4^{\text{geom}}}{2} \tag{13}$$

$$\frac{A_{4,Sh}^{TE\ geom}}{2} = \pi \cdot \left(\frac{D_4^2 - D_{4m,Sh}^2}{4} \right) \tag{14}$$

$$\frac{A_{4,H}^{TE\ geom}}{2} = \pi \cdot \left(\frac{D_{4m,H}^2 - D_{nut}^2}{4} \right) \tag{15}$$

The geometrical areas and diameters estimated from Equations (12) to (15) are used in corresponding effective equivalent nozzle area ($A^{TE}_{eff,i}$) of each branch while fitting the model. It is worth highlighting that Equation (8) also depends on the apparent efficiency of each branch. For that, the apparent efficiency values obtained by applying Equation (5) to each branch are used.

3.2. Dual-Volute Turbine

In dual-volute turbine, the flow path is designed in a way that each entry feeds separate sections of the rotor, due to the different volute lengths. Based on this different flow paths, the stator and rotor geometrical areas are estimated in different ways (see Figure 10). Doing this, it is appropriate to determine the mass flow parameter through the long and short volutes.

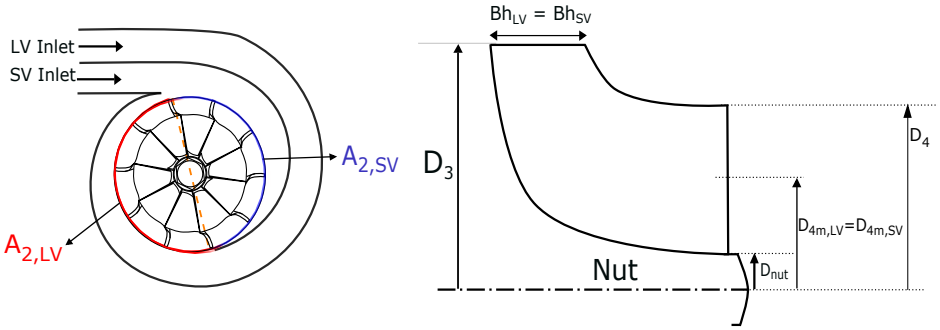

Figure 10. Geometrical description of dual-volute turbine (T#2DV).

As the flow is expanding at different sections of the rotor (Figure 10), the stator area is estimated by blade height (Bh) and half the wheel length ($(\pi/2) \cdot D_3$) for each volute, as shown in Equation (16). Similarly, the rotor outlet area of each volute is also determined by considering half the value of entire area, which is estimated using Equations (A4) and (17). It is due to the flow coming from each volute is not expanding through the entire circumference of the rotor. The rotor outlet diameter ($D^{DV}_{4m,i}$) is estimated in the same way as in vaneless turbines, as shown in Equation (11).

$$A^{DV\ geom}_{3,i} = \pi \cdot \left(\frac{D_3}{2}\right) \cdot Bh^{DV} \tag{16}$$

$$A^{DV\ geom}_{4,i} = \frac{A^{\text{geom}}_4}{2} \tag{17}$$

Once the effective equivalent nozzle area (Equation (8)) of each turbine entry of the turbocharger T#1TE and T#2DV is known, the reduced mass flow parameter in each branch can be calculated using the expression of the flow through an orifice with an isentropic expansion, as shown in Equation (18).

$$\dot{m}^{j}_{red,i} = A^{j}_{eff,i} \cdot \sqrt{\frac{\gamma}{R}} \cdot \left(\frac{1}{\Pi^{j}_{i,(0t,4)}}\right)^{\frac{1}{\gamma}} \cdot \sqrt{\frac{2}{\gamma - 1} \cdot \left[1 - \left(\frac{1}{\Pi^{j}_{i,(0t,4)}}\right)^{\frac{\gamma-1}{\gamma}}\right]} \tag{18}$$

3.3. Effective Area (A_{eff}) Fitting as a Function of MFR

Using the turbochargers T#1TE [12] and T#2DV (Figure 6), it is possible to study the behavior of the fitting coefficients of Equation (8) for both entries and with different mass flow ratios (MFR). The non-linear fitting procedure is performed individually using the individual performance map data of each turbine entry. These parameters are measured with the experimental method introduced in Section 2. The details about measurement procedures and data analysis can be read in [12]. They are calculated using Equations (2)–(7). Once the experimental reduced mass flow parameter of each entry is known, the experimental ($A^{j}_{eff,i}$) of each turbine inlet can be calculated by using Equation (18).

Equation (8) is then used to fit the values for a_i^j, b_i^j, c_i^j, and d_i^j coefficients for the whole turbine map of each entry with a least square method, which minimizes the root mean square error between the modeled and experimental values. By this, the coefficient values of Equation (8) are obtained, and these values for each turbine entry of the turbocharger T#1TE and T#2DV are plotted in Figure 11 versus the corresponding *MFR*. The analysis of individual map fitting coefficients of both entries of two turbochargers are detailed in Section 3.3 to obtain some physical trends.

Coefficient Analysis and Calibration

As mentioned above, the fitting is performed as two individual turbines with their corresponding turbine entry map data and, each *MFR* map has been fitted separately to study the behavior of the coefficients, as shown in Figure 11. It is worth highlighting that, according to the *MFR* definition in Equation (1), for an increasing *MFR*, the turbine mass flow parameter of the shroud/long volute entry increases and hub/short volute decreases.

- Coefficient *a*: It represents the rotor discharge coefficient as shown in Equations (8) and (19). The rotor effective flow area is variable with *MFR*, considering the amount of mass flow entering into each branch, i.e., growing as the mass flow grows, and this is true according to the definition of the discharge coefficient. Therefore, it is regarded as some quadratic behavior with *MFR* and the magnitude of this coefficient should be between 0 and 1. It is observed that the coefficient "*a*" trends are exactly as expected.

$$A_{4,i}^j = A_{4,i}^{j\ geom} \cdot a \tag{19}$$

- Coefficient *b*: The significance of this parameter is from velocity triangle speed ratio, and its order of magnitude can be estimated using Equation (20) as described in [30]. This coefficient is dependent on the mass flow passing through the turbine. More mass flow in a turbine branch gives higher "*b*" values than lower mass flow. This is due to higher radial velocities at rotor inlet, for the same peripheral speed and expansion ratio values. This trend is clearly shown in Figure 11c,d for both branches of every turbine type.

$$\begin{aligned} b &= \left(\frac{v_0}{C_{ss}}\right)^2 + \left(\frac{w_3}{C_{ss}}\right)^2 = \frac{A_{\text{eff}}}{A_0} \cdot \left(\frac{1}{\Pi_T}\right)^{\left(\frac{1}{\gamma}\right)} + O\left[10^{-1}\right] \\ &= O\left[10^{-1}\right] + O\left[10^{-1}\right] \rightarrow O\left[10^{-1}\right] \leq b \leq O\left[10^{0}\right] \end{aligned} \tag{20}$$

- Coefficient *c*: It is the ratio between rotor and stator discharge coefficients ("*a*" and "C_{Ds}"), as shown in Equation (21). As the effective flow area of the stator is variable with the mass flow ratio in the turbine, the value of "*c*" is expected to increase. Besides, "*c*" must always justify Equation (21), i.e., as an effective section introduced through the discharge coefficient (C_{Ds}) should not be higher than unity [30].

$$C_{Ds} = \left(\frac{a}{c}\right) \leq 1 \tag{21}$$

- Coefficient *d*: It is related to the pressure ratio in the rotor with respect to the total turbine pressure ratio [30]. Its value decreases with more flow into the branch and tends to 0.5. This implies that, with high mass flow in the branch, the pressure ratio in the rotor tends to be half of the total pressure ratio in the turbine. With low mass flow, most of the expansion is occurring in the rotor. Both are the expected logical trends.

Summarizing, all the coefficients values and trends with *MFR* have physical meaning, as they are derived from theoretical considerations [30]. These coefficients showed the exact expected trends with the various *MFR*s in both turbines, asymmetrical dual-volute and symmetrical twin-entry. By reviewing the fitting coefficients of each turbine entry of the two different radial in-flow types and for several *MFR*s in Figure 11, it is possible to impose those physical trends with *MFR*for each turbine

entry: a linear trend for coefficients "*b*", "*c*", and "*d*" and a quadratic behavior for "*a*". In this approach, seven coefficients of each turbine entry can be adjusted using a non-linear fitting method for all *MFR*s of a given branch at the same time. This implies that one single fitting procedure and one set of parameters will be needed for each entry of the turbine to predict the reduced mass flow in all flow admission conditions. Further elaborating this conclusion, only measuring three *MFR*s is enough for fitting the whole range of turbine mass flow parameter: any other non-measured *MFR*s can be predicted. The three most convenient *MFR*s to be measured in a gas stand are *MFR* = 0, *MFR* = 1, and *MFR* = 0.5 (partial admissions and full admission, respectively).

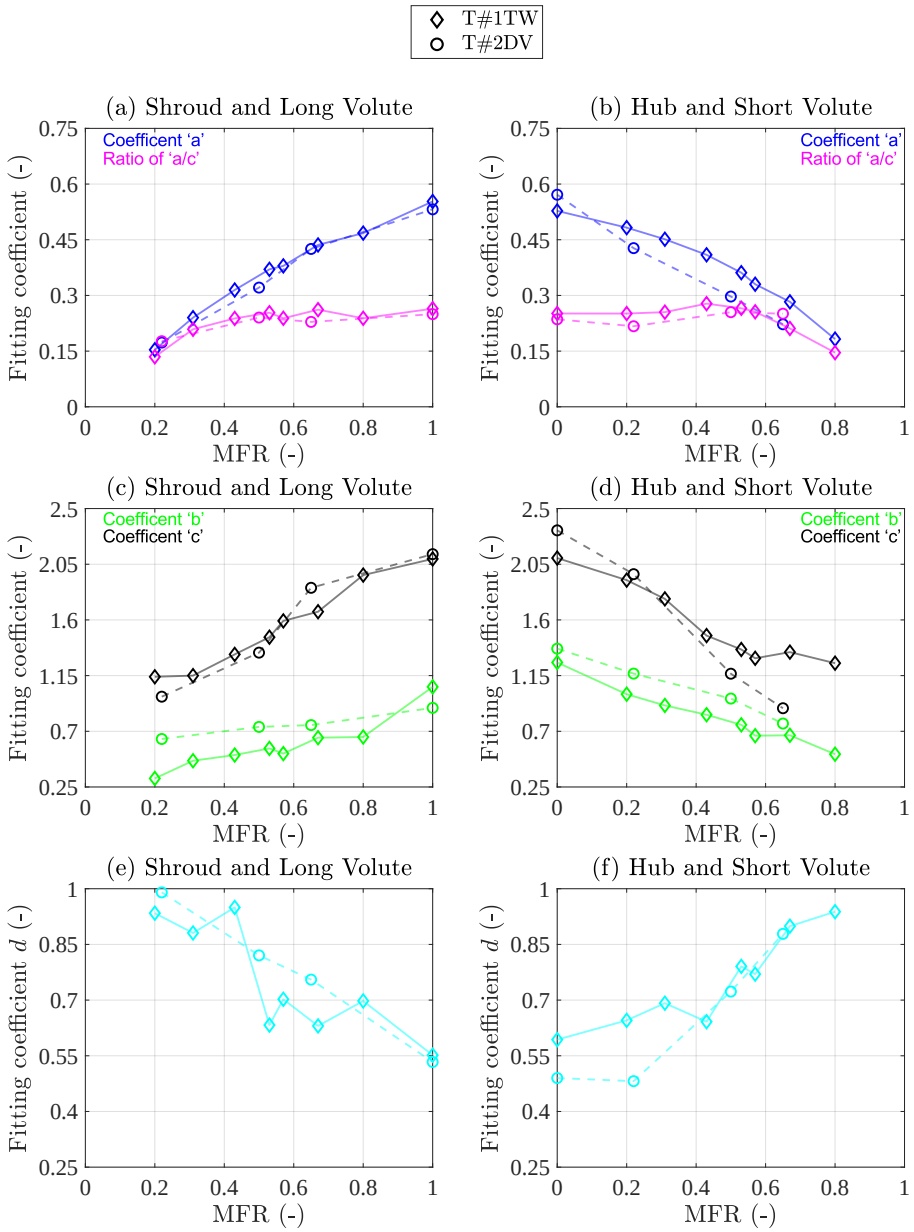

Figure 11. Reduced mass flow coefficients obtained using the individual *MFR* fitting for both T#1TE and T#2DV turbines. Each turbine entry map is fitted one by one.

Figure 12 shows the obtained results of the coefficients from a global fitting with *MFR* after imposing the discussed linear and quadratic trends. The first conclusion emerging is that the obtained trends are very similar between twin-entry and dual-volute turbines. It is an excellent result since initial values are mandatory for non-linear fitting procedures, and in this case the same set of initial values

can be used for fitting both types of turbines. In addition, being the tested turbines so different (twin symmetric vs. dual-volute asymmetric) it can assume that averaging for each branch the parameters set obtained in this paper (Table 2) is general enough to be used as initial values for the readers in their respective model calculation of another turbine.

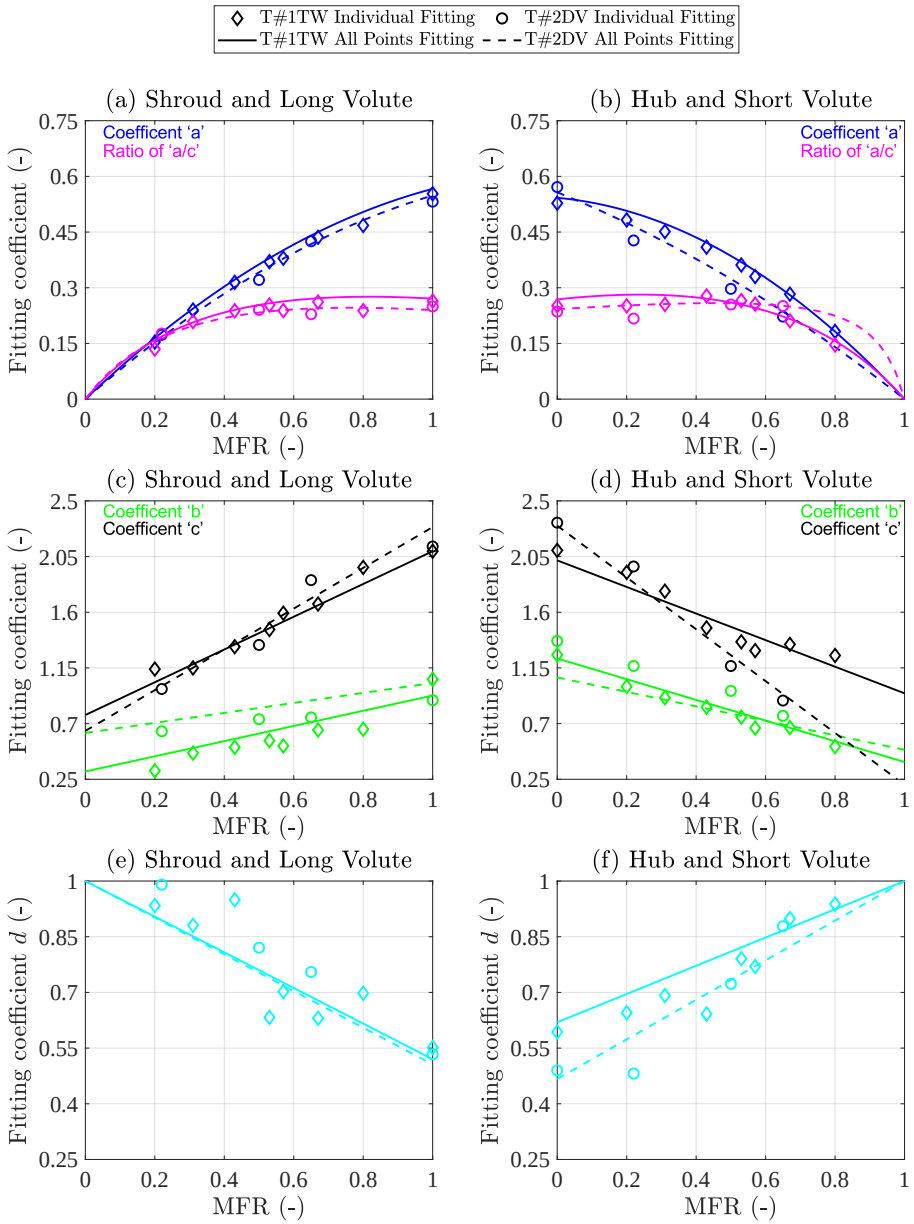

Figure 12. Reduced mass flow coefficient trends obtained using a global fitting procedure. Trends are imposed and all *MFR*s are fitted at the same time. The coefficients from individual *MFR* fittings are also shown for comparison.

The differences observed between T#1TE and T#2DV can be well explained by the effect of the asymmetry, i.e., T#1TE is symmetric between hub and shroud and T#2DV is not. In Figure 12a–d, this effect is especially evident in coefficients "a", "c", and "d" and does not show much for "a/c'. While in the twin turbine these coefficients (representing discharge coefficients) are quite symmetrical, this is not the case in the dual-volute with coefficient "a" at the short volute (Figure 12b). At the short volute, coefficient "a" shows lower values than at the long volute as the flow reduces (*MFR* increasing for the short volute) and coefficient "a/c" (representing stator discharge coefficient) does not show this

trend. The asymmetry effects are due to the volute tongue greatly affecting the rotor outlet discharge coefficient when compared to the stator outlet discharge coefficient.

Table 2. Reduced mass flow fitting coefficient trends value for T#1TE and T#2DV turbines obtained in a global fitting procedure.

Reduced Mass Flow Fitting Coefficient		T1#TE	T2#LV	T1#TE	T2#LV
		Shroud	Long Volute	Hub	Short Volute
$a_i^j = a_1 \cdot MFR^2 + a_2 \cdot MFR + a_3$	a_1	−0.3192	−0.2691	−0.4586	−0.1803
	a_2	0.8856	0.8176	−0.0837	−0.3768
	a_3	0	0	$-(a_1+a_2)$	$-(a_1+a_2)$
$b_i^j = b_1 \cdot MFR + b_2$	b_1	0.6134	0.4037	−0.8364	−0.5848
	b_2	0.3130	0.625	1.2262	1.0732
$c_i^j = c_1 \cdot MFR + c_2$	c_1	1.3234	1.6468	−1.0741	−2.0935
	c_2	0.7695	0.6412	2.0191	2.2996
$d_i^j = d_1 \cdot MFR + d_2$	d_1	−0.4799	−0.4938	0.3804	0.5332
	d_2	1	1	$(1-d_1)$	$(1-d_1)$

Figure 13a,b shows the model fitting results of two entries for the twin-entry (T#1TE) and dual-volute turbocharger (T#2D) with their corresponding coefficients, which are obtained using the global fitting process previously described. In Figure 13, it can be observed that the errors in modeling the reduced mass flow parameters of two turbine branches are small enough at various *MFR* (within ±5%) in both T#1TE and T#2DV turbochargers. Normalized reduced mass flow in the dual-volute case (Figure 13b) shows that RMS error for long volute is below 1.4% and for short volute below 0.5%. Therefore, it can be considered that the procedure explained above can be valid for other twin-entry or dual-volute turbochargers.

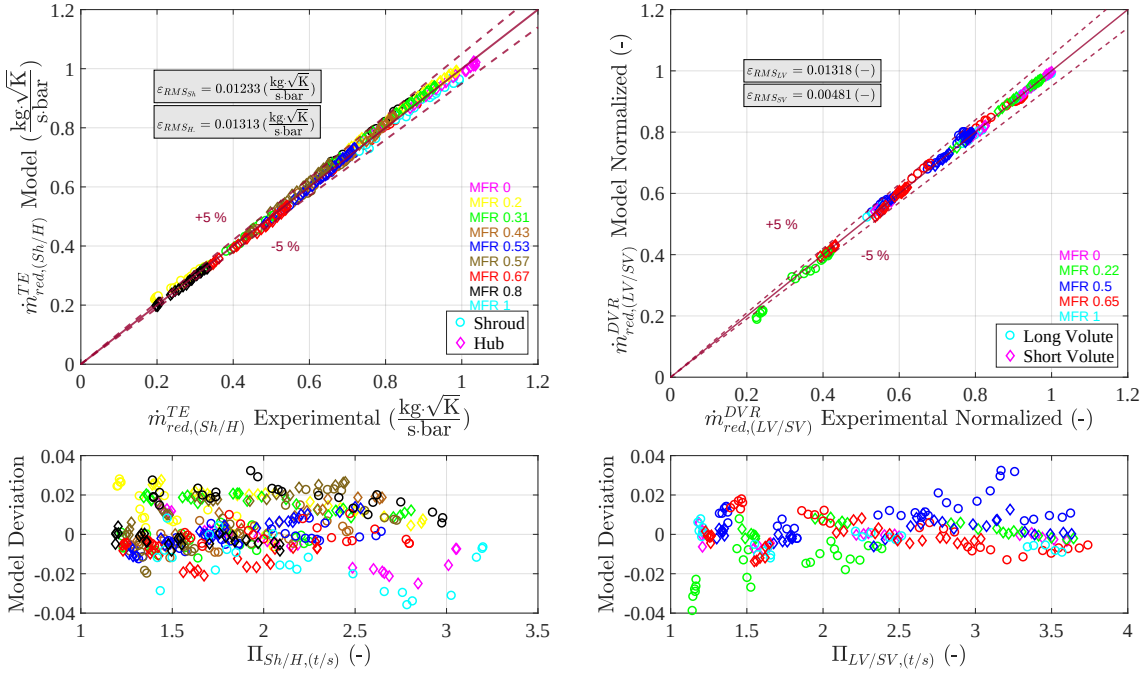

(**a**) Twin-entry (TE) turbocharger (T#1TE) (**b**) Dual-volute (DV) turbocharger (T#2DV)

Figure 13. Reduced mass flow Modeled versus Experimental for T#1TE and T#2DV turbochargers using the global fitting constants shown in Table 2.

The procedure for estimating a new turbine reduced mass flow map is as follows. Firstly, the seven initial values of fitting coefficients here proposed for each turbine inlet (seven for shroud and seven for hub or seven for long volute and seven for short volute, depending on turbine type) need to be provided for the non-linear fitting procedure. Values provided in Table 2 can be used as an example of initial values for non-linear fitting calculation. Further, the final values can be obtained with the corresponding effective area ($A^j_{eff,i}$), geometries, and the turbine map data. After the fitting, the model can calculate the reduced mass flow for any non-measured *MFR*, reduced speed, and pressure ratio, even for far-off non-measured conditions by substituting the fitted $A^j_{eff,i}$ in Equation (18).

4. Efficiency Fitting Using VGT Model

In the case of efficiency fitting, the model described in Appendix A and [30] is re-designed in a similar way to the reduced mass flow fitting procedure. The efficiency equation (Equation (22)) (hereafter called apparent efficiency) is fitted independently for each entry of the turbine. As aforementioned, the turbochargers used in this study are vaneless turbines; accordingly, the VGT model is modified. The stator flow outlet angle (φ_2^{flow}) is no longer guided by blades as in VGT turbine model; accordingly, the $K_2^\star$ term is expressed as shown in Equation (24). However, in z_i^j (Equation (25)), the set of each turbine maps depending on the *MFR* are provided. It is a first and straightforward adaption of Equation (A15) and the model explained in [30].

$$\eta^j_{i,\,(t/s)} = -K_1 \cdot \left(\sigma_i^j\right)^2 + K_2^\star \cdot \left[1 - \frac{K_3}{\left(\sigma_i^j\right)^2}\right]^{\frac{1}{\gamma-1}} \cdot \left(\sigma_i^j\right) \tag{22}$$

$$K_1 = 2\left(\frac{r^j_{4,i}}{r^j_3}\right)^2 \tag{23}$$

$$K_2^\star = 2\frac{A^j_{eff,i}}{A^{j\ geom}_{0,i}}\left(z_i^j \cdot \tan\alpha^{j\ \text{flow}}_{3,i} + \sqrt{\frac{K_1}{2}} \cdot \tan\beta^{j\ metal}_{4,i}\right) \tag{24}$$

$$z_i^j = -(a_i'^j \cdot n^j_{red,i} + b_i'^j) \cdot \sigma_i^j + (c_i'^j \cdot n^j_{red,i} + d_i'^j \cdot MFR^{j^2} + e_i'^j \cdot MFR^j + f_i'^j) \tag{25}$$

Nevertheless, in vaneless turbines, the volute or casing will take over the function of flow guidance at the entry to a rotor in addition to flow distribution and acceleration [13]. Therefore, a physical definition based on the geometry for a compressible flow has been considered according to Watson and Janota [13], to calculate the rotor inlet gas angle (α_3^{flow}) for vaneless turbines, as shown in Equation (26).

$$\tan\alpha_3^{\text{flow}} = \frac{r_0 \cdot \rho_3 \cdot 2\pi \cdot B_h \cdot C_{Dr3}}{A_0 \cdot \rho_0 \cdot C_{D0}} \tag{26}$$

Just for calculating this flow angle, it was assumed that the discharge coefficient at the tongue (C_{D0}) (station 0 in Figure 14) is similar to the radial discharge coefficient (C_{Dr3}) and, therefore, their ratio is very close to 1. For estimating the density ratios shown in Equation (26), an iterative procedure should be used; to avoid this, an isentropic expansion between stations 0 and 3 was assumed. Then, the density ratio can be expressed as a function of pressures ratio (p_3/p_0). However, the pressure ratio between stations 0 and 3 is not available in the turbine maps, thus an additional assumption is made at this point for this particular purpose. Equation (9) can be used to express the isentropic expansion between stations 0 and 3, as shown in Equation (27). It can be noted that coefficient "*d*" in Equation (9) comes from the reduced mass flow fitting and it represents the pressure ratio in the rotor with respect to the total turbine pressure ratio.

$$\frac{\rho_3}{\rho_0} = \left(\frac{p_3}{p_0}\right)^{\frac{1}{\gamma}} = \left(\frac{1 + d_i^j \cdot \left(\Pi_{i,(0t,4)}^j - 1\right)}{\Pi_{i,(0t,4)}^j}\right)^{\frac{1}{\gamma}} \tag{27}$$

Therefore, Equation (26) can now be expressed as Equation (28) for both branches and it should be calculated with their corresponding turbine entry geometry and expansion ratios according to the assumption of two turbines modeling.

$$\tan \alpha_{3,i}^{j\ \text{flow}} = \left(\frac{r_{0,i}^j \cdot 2\pi \cdot B_{h,i}^j}{A_{0,i}^j}\right) \cdot \left(\frac{1 + d_i^j \cdot \left(\Pi_{i,(0t,4)}^j - 1\right)}{\Pi_{i,(0t,4)}^j}\right)^{\frac{1}{\gamma}} \tag{28}$$

In Equation (28), $A_{0,i}^j$ is the area at the tongue of each branch, $B_{h,i}^j$ is the blade height of each branch, and $r_{0,i}^j$ is the radius of the centroid of section $A_{0,i}^j$, as shown in Figure 14. In this manner, the rotor inlet gas angle (α_3^{flow}) for vaneless twin-entry or dual-volute turbines can be approximated.

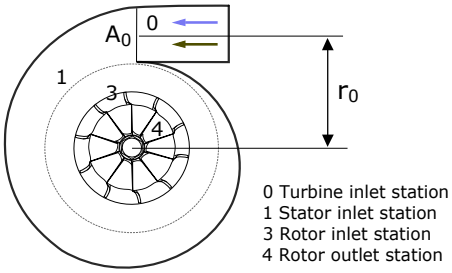

Figure 14. Geometrical description for calculating the flow angle in vaneless twin-entry/dual-volute turbines.

Figure 15 illustrates the variation of the rotor inlet flow angles with the total to static turbine expansion ratio of each turbine branch. Here, the results are corresponding to the twin-entry turbine T#1TE [12]. In Figure 15, it can be observed that as the flow in Shroud or Hub branch is increasing, the flow angle becomes lower. At *MFR* 0.2 (yellow circled points) and *MFR* 0.8 (black diamond points) conditions, the flow is lower in Shroud and Hub branches respectively. The flow angle values are higher and shows a continuous reduction of their values from lower to higher turbine expansion ratios.

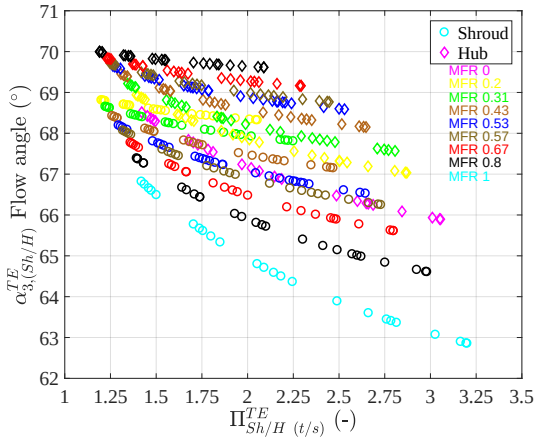

Figure 15. Rotor inlet flow angles at different flow admission conditions for Shroud and Hub branch of T#1TE.

It is noteworthy that the K_1 term in Equation (22) is dependent on the ratio of rotor outlet radius of each branch ($r^j_{4,i}$) and turbine wheel radius (r^j_3). For this, the geometry simplifications of twin-entry and dual-volute turbines as demonstrated above for fitting the reduced mass flow model are also considered in fitting the apparent efficiency.

In this way, the apparent efficiency model has been fitted separately for each branch of the twin-entry turbocharger using the data of whole turbine map to analyze the behavior of the coefficients for each turbine branch with *MFR*. Accordingly, a set of coefficients for each *MFR* of the individual twin-entry turbine [12] branch is obtained, as shown in Table 3. It is evident that the model does not show any clear trends with the mass flow ratios (e.g., the reduced mass flow fitting parameters), except that coefficients d'^j_i and e'^j_i tends to zero in all the *MFR* for both branches. In addition, the value of the coefficient a'^j_i is close to zero for many *MFR*s.

Figure 16 shows the model results of both branches at different *MFR* by using the coefficients from Table 3. The results are coherent with the experimental data of each branch with an average root mean square error of 0.02017 for both branches together (separate RMSE for each branch can be read at Figure 16). Furthermore, the model is sufficient to extrapolate until off-design conditions of each turbine branch map with there corresponding *MFR* fitting constants from Table 3. However, this model has a limitation that it is not potential to extrapolate to non-measured *MFR*s and reduced turbine speed as compared to the reduced mass flow model. This is because of the coefficients do not show any apparent trends with the *MFR*. Consequently, in this paper, the model has been improved to enable extrapolating to non-measured *MFR*s and speeds of twin-entry/dual-volute turbochargers. The procedure to refine the model is based on the analysis of twin-entry turbocharger experimental data.

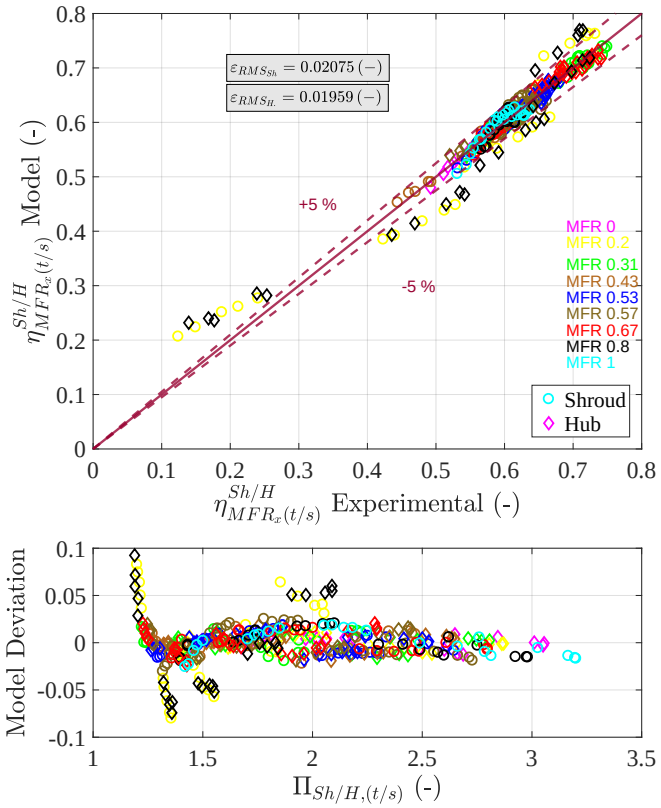

Figure 16. Comparing the apparent turbine efficiency results from VGT turbine model with the experimental values for T#1TE turbocharger. Each *MFR* map is individually fitted for the respective turbine branch.

Table 3. Apparent efficiency fitting coefficients from Equation (25) for each turbine branch of T#1TE [12]. Every *MFR* map is fitted individually.

MFR_x	Branch	a'^{TE}	b'^{TE}	c'^{TE}	d'^{TE}	e'^{TE}	f'^{TE}
0	Sh	—	—	—	—	—	—
	H	0.0205	1.4095	0.1379	0	0	0.6572
0.2	Sh	0.1349	0.3864	0.4552	0	0	3.850×10^{-14}
	H	2.313×10^{-14}	1.064	0.0854	0	0	0.6612
0.31	Sh	0.1443	0.0180	0.2638	0	0	0.3116
	H	2.238×10^{-14}	0.9210	0.0768	0	0	0.6227
0.43	Sh	0.1380	0.0501	0.2382	0	0	0
	H	1.496×10^{-13}	0.8709	0.0678	0	0	0.7276
0.53	Sh	2.228×10^{-14}	0.7188	0.1006	0	0	0.5424
	H	3.994×10^{-14}	0.7276	0.0551	0	0	0.8262
0.57	Sh	2.220×10^{-14}	0.7060	0.0814	0	0	0.6297
	H	0.1508	4.441×10^{-14}	0.2012	0	0	0.1183
0.67	Sh	2.515×10^{-14}	0.8564	0.1024	0	0	0.5150
	H	0.1416	7.668×10^{-11}	0.1990	0	0	0.3941
0.8	Sh	2.869×10^{-14}	1.0488	0.1160	0	0	0.5362
	H	0.0205	0.5535	0.5070	0	0	5.038×10^{-12}
1	Sh	2.222×10^{-14}	1.4958	0.1515	0	0	0.6301
	H	—	—	—	—	—	—

5. Proposed Model for Twin-Entry and Dual-Volute Turbines

5.1. Mixed Flow Approach

According to the assumption of two entries as an individual turbine, the apparent efficiency of each turbine branch is estimated with the enthalpy difference. This difference is between the turbine scroll inlet temperature and the mix of temperatures that is available at the outlet of a turbine as shown in Equation (6) and Figure 17. However, at the rotor outlet, temperatures coming from the individual turbine branch will be different under full and unequal flow admission conditions. This is due to the different expansions of the flow with their given efficiencies in each branch [12].

Meanwhile, the turbine operating under partial admission conditions (*MFR* 1 or 0 (i.e., all flow in one of the entry by blocking the other and vice versa)) the power produced by the turbine is only due to that working branch (Entry 1 or 2). Besides, in these conditions, there is only one turbine outlet temperature , which is easy to measure in the gas stand.

Therefore, the first hypothesis tested, the turbine outlet temperature in all the admission conditions can be calculated using only the extreme flow cases (*MFR* 0 and 1) as two individual turbines. Based on the T#1TE turbocharger fitting results in Table 3, the coefficients which trends to zero ($a_i'^{TE}$, $d_i'^{TE}$ and $e_i'^{TE}$) are avoided in further analysis. For that reason, only 3 fitting parameters ($b_i'^{TE}$, $c_i'^{TE}$ and $f_i'^{TE}$) of each branch are used in Equation (25). These parameters are fitted again for the apparent efficiency (Equation (22)) for partial flow admission cases. Figure 18 shows the extrapolation of extreme flow cases for shroud and hub branch of twin-entry turbine T#1TE [12], using the individual fitting constants of *MFR*0 and 1 in Table 4 and combining them in Equation (29) for efficiency. In addition, the global fitting constants of reduced mass flow of each branch shown in Figure 12 and Table 2 are used for mass flow parameters calculation. Equation (29) shows the parameters that account for angle incidence losses in the flow oriented model. These are the only losses of the model in Equation (22), apart from the discharge coefficients accounted by the flow model. Equation (29) shows how the incidence losses depend linearly of both reduced speed and blade to jet speed ratio.

$$z_i^{TE} = -(b_i'^{TE} \cdot \sigma_i^{TE}) + (c_i'^{TE} \cdot n_{red,i}^{TE}) + f_i'^{TE} \tag{29}$$

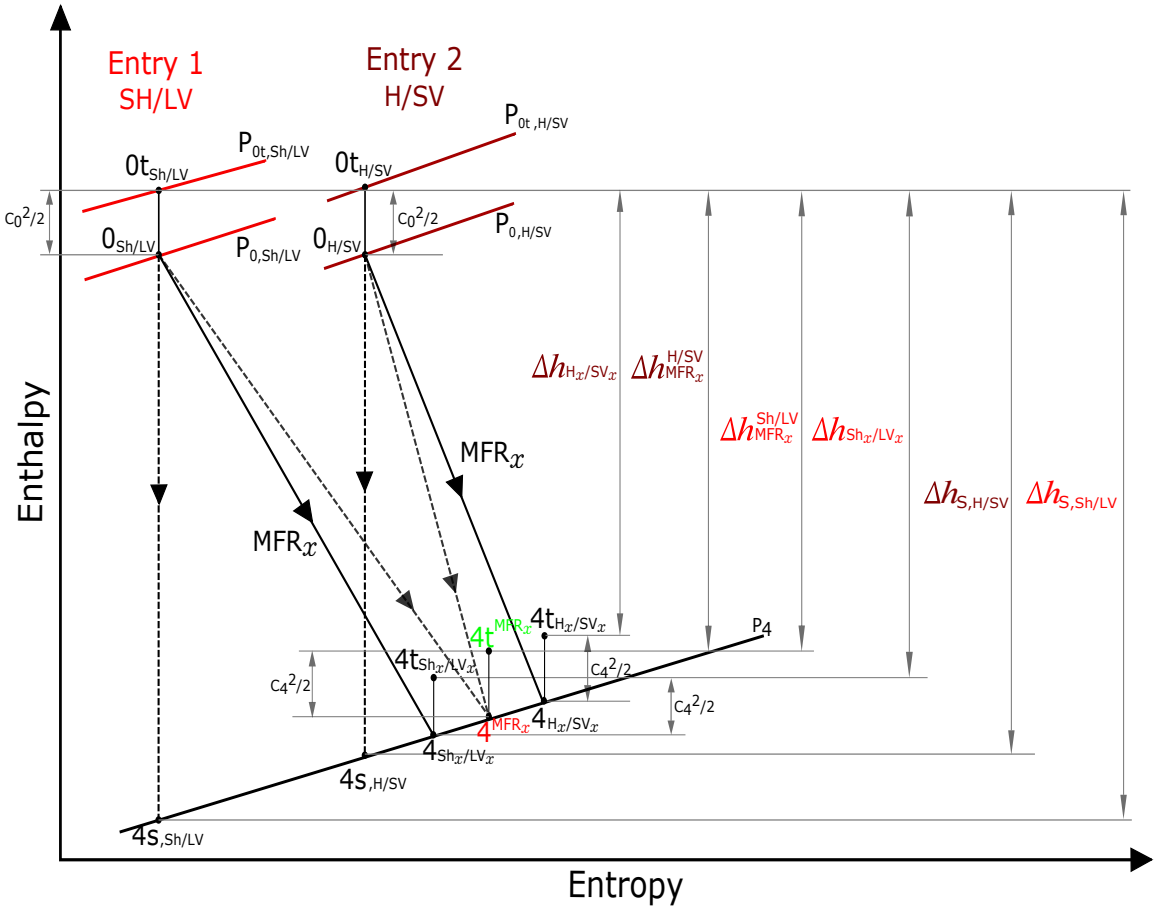

Figure 17. Twin-entry/dual-volute radial turbines expansion process in partial admission conditions.

Table 4. Fitting coefficients of partial admission conditions using apparent efficiency.

MFR_x	b'^{TE}	c'^{TE}	f'^{TE}
0 (H)	1.4685	0.1493	0.6280
1 (Sh)	1.4278	0.1189	0.6895

A methodology proposed by Payri et al. [43] has been used to extrapolate the partial admission maps. Figure 18 shows that the accuracy is good and can be noted that the hub branch with a higher trimming (with a higher rotor inlet to outlet radius ratio) shows a significant difference in mass flow parameter between different reduced speeds for a given pressure ratio. It means a higher work in the centrifugal forces field than the Shroud branch with a lower radius ratio. Figure 18 also shows slightly higher peak efficiency at Hub branch, probably due to the higher trimming (higher specific work) and the lower tip leakage losses when the flow is concentrated in hub branch than in shroud [44,45].

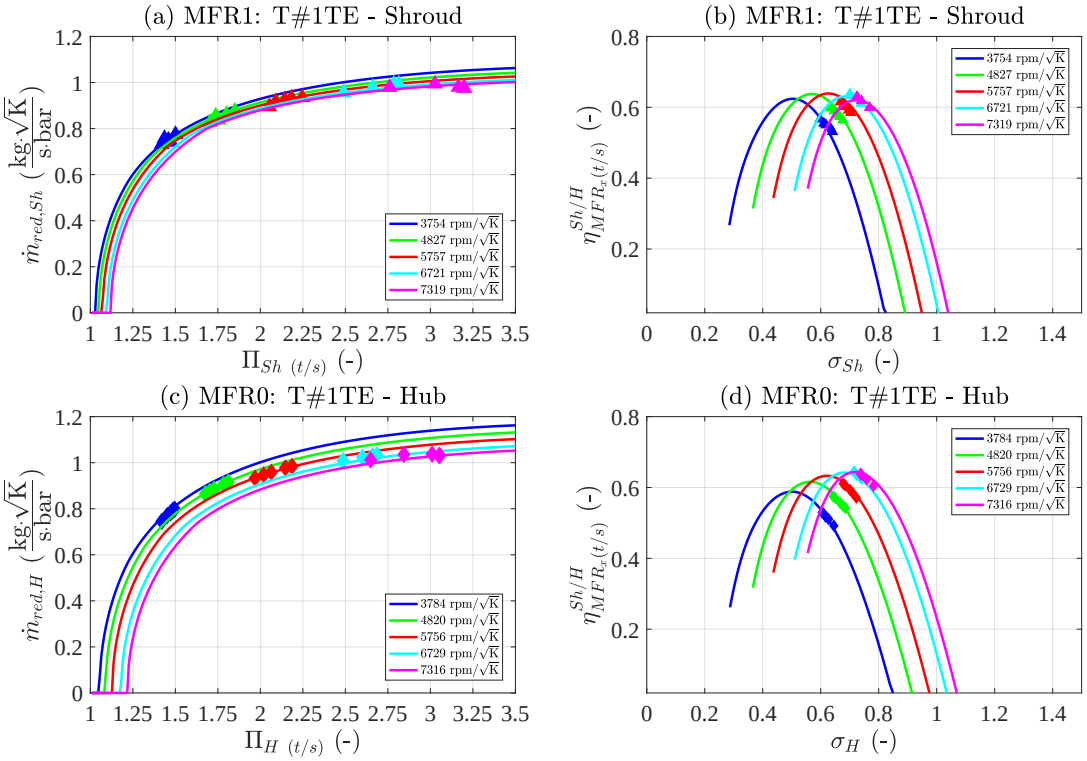

Figure 18. Extrapolation of partial admission conditions for T#1TE (*MFR* 0 and 1).

For predicting the same turbine outlet temperature as in experiments at different flow admission conditions, a look-up table is generated with the extrapolated efficiency, blade to jet speed ratio, and reduced turbine speeds of *MFR* 0 and 1 separately, corresponding to hub and shroud entries in the turbine T#1TE. Eventually, if every other flow admission condition (*MFR*s other than 0 or 1) is merely a quasi-steady mass average of what happens at *MFR* 0 and *MFR* 1. It is possible to calculate the static turbine outlet temperature ($T_{4,i}^{TE}$) using Equation (30). Here, $\eta_{i,\,(t/s)}^{TE}$ is the estimated efficiency of every *MFR* (either 0 or 1, for Hub or Shroud branches, respectively) at every BSR and every reduced speed obtained from extrapolated efficiencies of partial admission conditions shown in Figure 18.

It is worth checking that, in the case of partial admission conditions, the estimated temperatures using Equation (30) should be equal to the experimental temperature values and, the same can be seen in Figure 19. It is important to note that the temperatures are very symmetrical between *MFR* 0 and 1 in all turbine reduced speeds.

$$T_{4,i}^{TE} = T_{0t,i}^{TE}\left[1 - \eta_{i,\,(t/s)}^{TE}\left(1 - \left(\Pi_{i,(0t,4)}^{TE}\right)^{\frac{1-\gamma}{\gamma}}\right)\right] - \frac{c_4^2}{2\,c_p} \tag{30}$$

To check the validity of this approach, the mixed static turbine outlet temperature in full and unequal admission conditions is estimated as a mass-weighted average between the individual turbine outlet temperature (Equation (30)), as shown in Equation (31). As flow expansion from each branch finishes in a common turbine outlet station, the individual turbine outlet temperatures after the expansion are mixed depending on the flow passing through each inlet. In fact, from the gas stand, the mixed temperature is the only information available at the turbine outlet station throughout full and unequal flow admissions at the turbine inlet.

$$T_4^{MFR_x} = T_{4,Shx}^{TE} \cdot MFR_x + T_{4,Hx}^{TE} \cdot (1 - MFR_x) \tag{31}$$

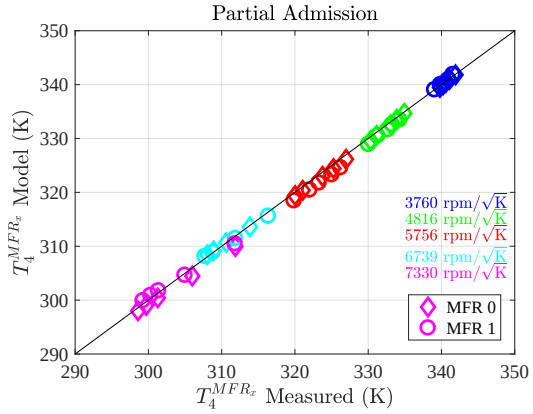

Figure 19. Estimated turbine outlet temperature using extrapolated maps of *MFR*0 and 1 for T#1TE.

In Figure 20, it can be observed that the prediction of temperatures using the mixed flow approach (Equation (31)) is always higher for unequal and full flow admissions. Moreover, Figure 20 also shows an additional aspect that the prediction of temperatures is nearly symmetrical between specific *MFR*s with respect to *MFR* = 0.5 (see Figure 20a–c) and also the error was maximum at *MFR* = 0.5. The difference between estimated mixed temperature and experimental values were further investigated with *MFR* and a new parameter MFR'_x, as shown in Equation (32); this is done to observe the symmetry with respect to the *MFR*= 0.5.

Figure 21 shows the temperature prediction error ($\Delta T_4^{MFR_x}$) for all the MFRs and reduced turbine speeds. Based on Figure 21a,b, the following conclusions can be made:

- The error is substantially zero for both partial admission conditions, as there are no mixing of flows at the outlet branch of the turbine. Moreover, the deviation of the error in *MFR* 0 and 1 is quite symmetrical to *MFR* 0.5.
- The errors are always positive in the case of unequal and full admission flows. It is understood that the proposed mixed approach is always under-predicting the apparent efficiency. The error is lower at highly uneven flows between branches and maximum around full admission, i.e., increasing from low unbalanced flows (i.e., *MFR* 0.2 and 0.8) to having same flows (*MFR* 0.5) in both branches.
- The parameter MFR'_x given in Equation (32) shows a significant turbine outlet temperature error as nearly symmetric and equally far from full admission conditions, as demonstrated in Figure 21b. In this figure, the error tends to be lower (efficiency lower) when new parameter MFR'_x is equal to 0.5 and higher (efficiency higher) when it is similar to zero.
- The reasoning for always positive errors can be explained as losses due to the sudden expansion of flows when the turbine is working only with one branch while the other is blocked; in these conditions, the flow also expands into a non-flow branch. As a consequence, this gives the lower efficiency as compared to the turbine operating with two branches together at different flow admissions.
- Having the two turbines individually for each inlet with an extreme flow condition and predicting the situations of other flow admissions by a mixing approach always produces higher temperatures. The efficiency losses for the individual turbines are added through the mixing method and increase the entropy of the turbine flow.
- In adiabatic calculations, the outlet temperature represents more or less efficiency; as a result, a higher temperature gives a lower performance. The best conditions are those where the $T_4^{MFR_x}$ error is always higher and which corresponds to having the highest flow in the hub branch and also having the same mass flow in both branches (according to Figure 21); this is especially true at low turbocharger speeds (blue colors in Figure 21). Thus, it means that the losses between both

branches of the twin-entry turbine are maximum when there is no flow in one of the branches. As the flow conditions are changing from partial to full admission state, the efficiency is better.

From the above conclusions, it can be understood that, having a calibration function, it is possible to reduce the error and obtain the same outlet temperature as in the experimental points in all flow conditions. Once the right mixed turbine outlet temperature is known, the model will have the capabilities of predicting the proper efficiency of each branch in all flow situations.

$$MFR'_x = |MFR_x - 0.5| \tag{32}$$

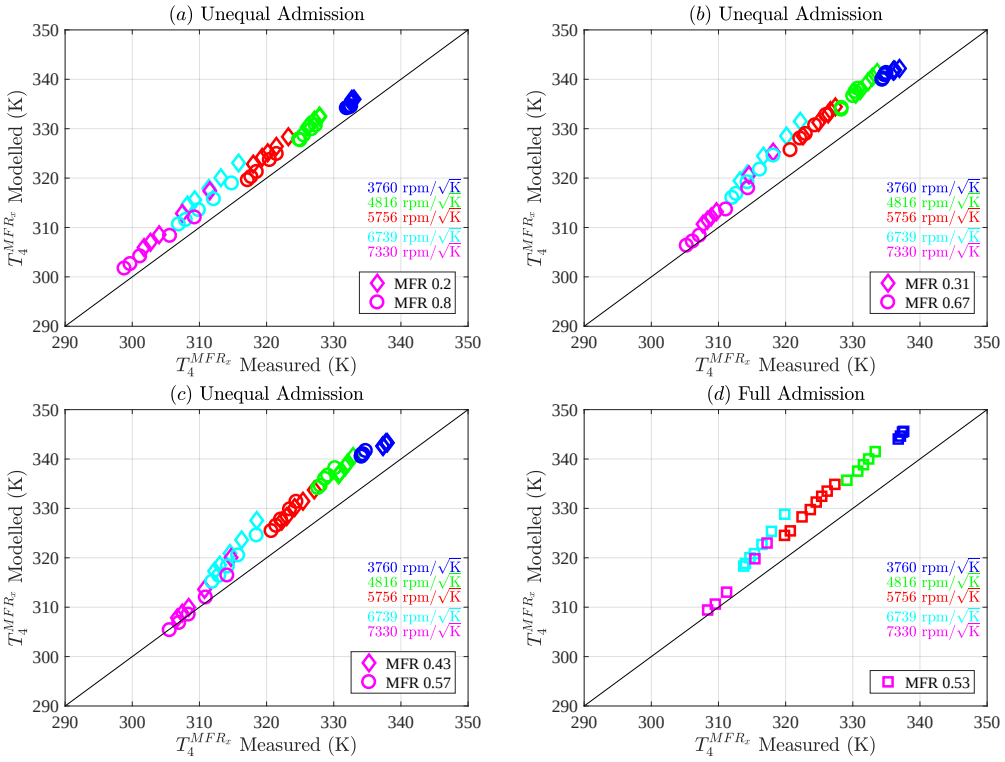

Figure 20. Estimated mixed turbine outlet temperature for full and unequal flows using extrapolated maps of *MFR* 0 and 1 for T#1TE.

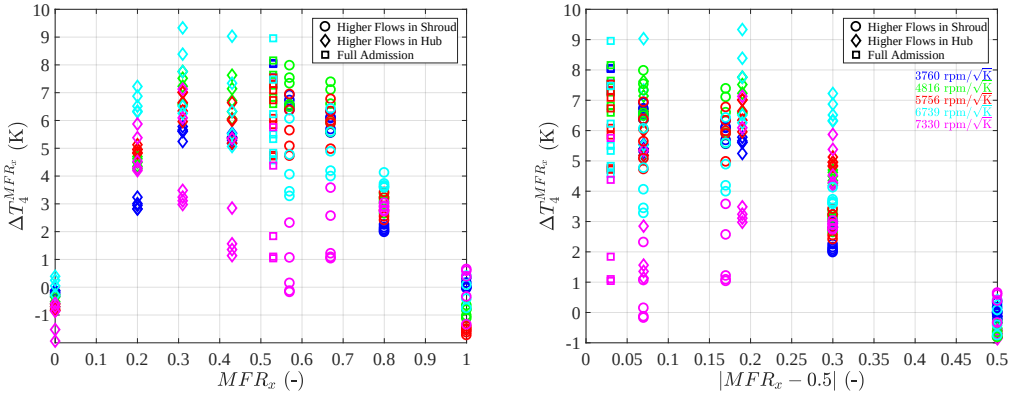

(**a**) (**b**)

Figure 21. Error prediction in all admission conditions using the extreme flow maps for T#1TE. (**a**) Mixed turbine outlet temperature error with MFR, (**b**) Mixed turbine outlet temperature error with MFR'_x.

5.2. Mixed Flow Approach Corrected

Based on the outcome of mixed outlet temperatures in all the admission conditions in Section 5.1, it is clear that a fitting parameter can be feasible for adjusting the error ($\Delta T_4^{MFR_x}$) generated by the mixed flow approach in the case of full and unequal flow admissions. In a way that is appropriate to reduce the error, more analysis was done with variables such as a blade to jet speed ratio (BSR), MFR_x, and reduced turbine speed, as shown in Figure 22.

If the error is examined against MFR_x parameter and turbine reduced speed, as shown in Figure 22a,b, respectively, the error shows a comparatively parabolic trend with reduced turbine speed and also the error decreases from full admission to partial admission conditions. Furthermore, if the error is observed with the blade to jet speed ratios of each branch for a different MFR_x, as shown in Figure 22c, the error shows a logarithmic trend with MFR_x parameter and also moderately linear as BSR grows. Besides, if the error is compared with the similar reduced turbine speed of all the flow admission conditions, as shown in Figure 22d, the y-intercept values shows a parabolic dependency with the same reduced turbine speed for different *MFR*s and BSR. Moreover, in Figure 22, it is also clear that the observed trends can agree with MFR'_x, as this parameter shows that the error is symmetric, as shown in Figure 22b. It should be taken into account that the trend of the error in $T_{4,TE}^{MFR_x}$ is the same than the trend of any correction coefficient designed to increase the efficiency at unequal and full admission conditions, in order to reduce error. By considering all these, a new fitting function (z'^j) is proposed, as shown in Equation(33), because of the noticed trends shown in Figure 22. Equation (33) is a term that is used to correct angle incidence losses, by reducing them in the light of new findings, in the flow oriented efficiency model of Equation (22). For z'^j, five fitting coefficients are introduced, which are the same for both branches. It is worth noting that the term z'^j becomes zero at $MFR_x = 0$ or $MFR_x = 1$ since in this cases the error in temperature does not exist and efficiency is not under-predicted.

$$z'^j = \left(MFR'_x - 0.5\right) \cdot \ln\left[\left(MFR'_x\right)^{k_0^j} + k_1^j \cdot \sigma_i^j\right] \cdot \left[k_2^j + k_3^j \cdot \sigma_i^j \cdot n_{red,i}^j - \frac{k_4^j \left(n_{red,i}^j\right)^2}{\left(MFR'_x + \sigma_i^j\right)}\right] \tag{33}$$

The proposed fitting function (z'^j) is added to the old z_i^j function (Equation (29)), as shown in Equation (34).

$$z_i^j = -\left(b_i'^j \cdot \sigma_i^j\right) + \left(c_i'^j \cdot n_{red,i}^j\right) + f_i'^j + z'^j \tag{34}$$

It is important to note that the final z_i^j function, Equation (34), has 11 fitting coefficients in total for the two branches: three coefficients for each branch ($b_i'^j$, $c_i'^j$, and $f_i'^j$) obtained from data at $MFR_x = 0$ and $MFR_x = 1$ and further kept constant in the mixed flow approach and five coefficients (k_0^j, k_1^j, k_2^j, k_3^j, and k_4^j) of z'^j that are associated to correct the extra losses (not real) generated by the mixed flow approach. Now, Equation (34) is used in Equation (24) as well as in Equation (30). As a result, the final $T_4^{MFR_x}$ (Equation (31)) is now calculated with z'^j for reducing losses (Equation (34)) apart from partial admission conditions. In summary, all 11 fitting coefficients are globally fitted together for both branches using a non-linear fitting procedure by using all the partial, unequal, and full admission flow data of each branch of T#1TE. It is worth highlighting that z'^j is equal to zero while fitting the partial admission conditions (MFR_x 0 or 1); consequently, the coefficients obtained while fitting the partial admission data should be similar to coefficients shown in Table 4. Table 5 shows the values of 11 fitting coefficients obtained while fitting the mixed turbine outlet temperature.

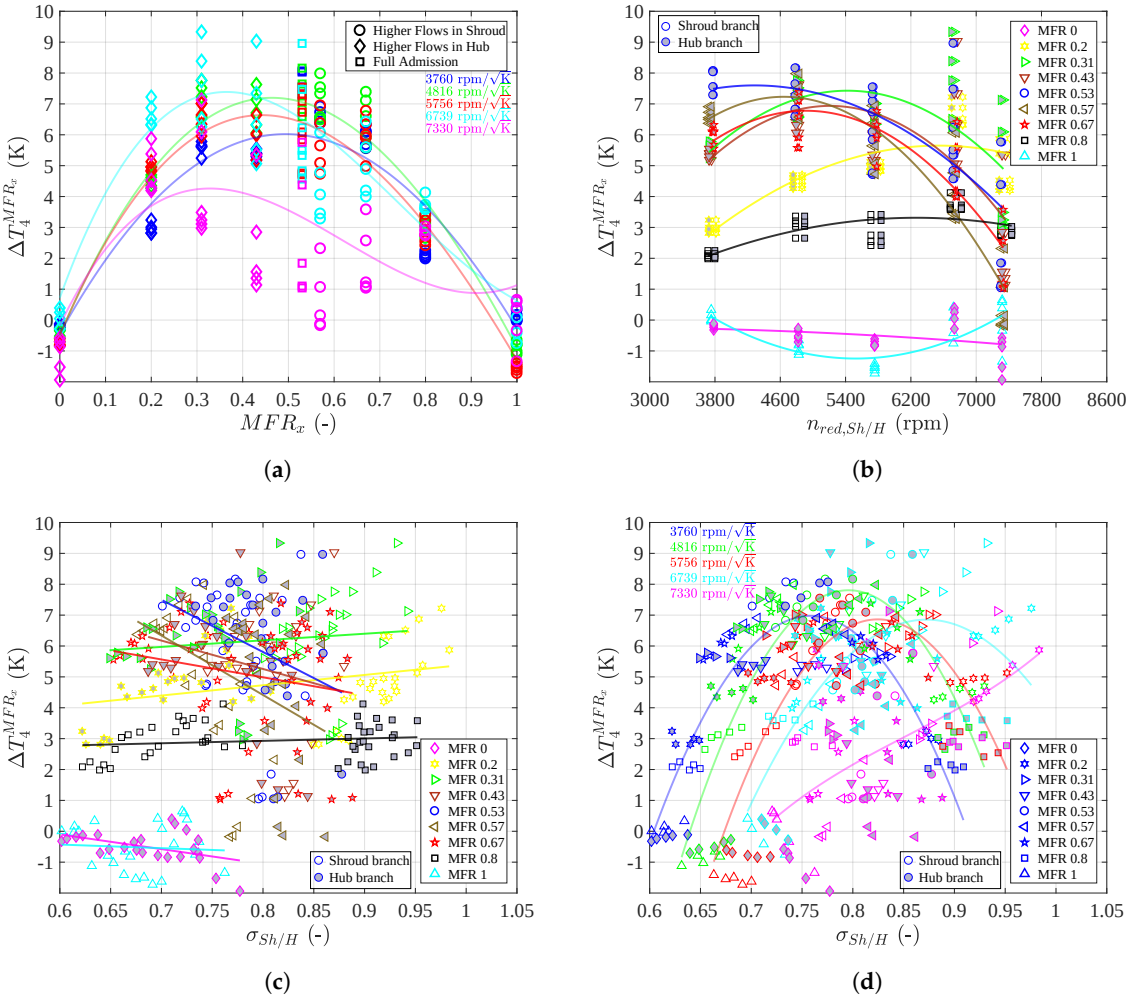

Figure 22. Analysis of T#1TE turbine outlet temperature error with different parameters in order to find an a correction function to reduce the error. (**a**) Error with MFR_x and same reduced turbine speeds, (**b**) Error with reduced turbine speed of each branch and MFR_x, (**c**) Error with the BSR of each branch and MFR_x, (**d**) Error with same reduced turbine speed for different MFR_x and BSR.

Table 5. Fitting coefficients of mixed turbine outlet temperature correction with new fitting function for T#1TE.

MFR_1 (Sh)			Fitting Function (z'^{TE})					MFR_0 (H)		
b'^{TE}_{Sh}	c'^{TE}_{Sh}	f'^{TE}_{Sh}	k^{TE}_0	k^{TE}_1	k^{TE}_2	k^{TE}_3	k^{TE}_4	b'^{TE}_{H}	c'^{TE}_{H}	f'^{TE}_{H}
1.4685	0.1493	0.6280	4.9408	0.0330	0.1386	0.0495	5.135E-03	1.4278	0.1189	0.6895

Figure 23 shows the level of correlation between the mixed turbine outlet temperature measured in the gas stand and modeled $T_4^{MFR_x}$ values for all the mass flow ratios data points in the map of twin-entry turbine (T#1TE). It can be observed that modeled $T_4^{MFR_x}$ values show good accordance with the experimental points, which is evidenced by a Root Mean Square Error (RMSE) of 1.3518 (K). By using the proposed fitting function (z'^j) within the $K_2^\star$ term of the apparent efficiency equation (Equation (24)), it is possible to obtain the mixed turbine outlet temperature of all the *MFR*s only with the 11 fitting coefficients shown in Table 5 and the 14 flow coefficients shown in Table 2. The efficiency model is a flow oriented model and both must be fitted together. Once the outlet temperature values are predicted well, these values can be used to obtain the apparent efficiency of each branch.

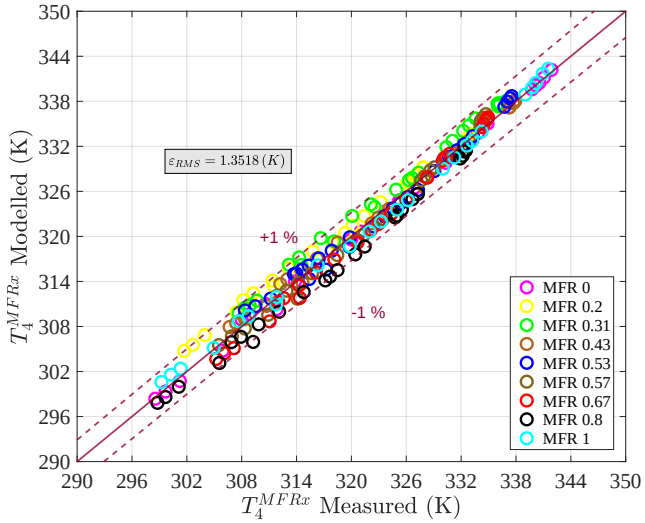

Figure 23. Comparing the prediction of modeled mixed turbine outlet temperature with experimental values for T#1TE turbocharger.

5.3. From Mixed Flow Corrected Approach to Apparent Efficiency Merit Functions

In Section 5.2, it is shown that the mixed turbine outlet temperatures can be well predicted by adding the suggested calibrated function in Equation (29), as shown in Equation (34). However, most of the time, the double entry turbine maps will be in terms of apparent efficiency either adiabatic or adiabatized from standard gas stand maps [46]. Therefore, one must find the relation between real efficiencies calculated with the corrected mixed flow approach and the apparent efficiencies measured in the gas stand, instead of that with measure outlet mixed flow temperatures. With this approach, it is now possible to use the final $T_4^{MFR_x}$ (Equation (31)) in Equation (35) to obtain total temperature and later on in apparent efficiency definition in Equation (5) to estimate the efficiency values similar to the experiments. By continuing the simplification of apparent efficiency (Equation (5)) using the final $T_{4t}^{MFR_x}$ for both branches, it is possible to obtain the final apparent efficiency expressions for both branches as shown in Equations (36) and (37). It is worth noting that the final formulation shown in Equations (36) and (37) are a function of actual efficiencies (not apparent), expansion ratios, and total inlet temperature of both turbine branches to follow the mixed flow corrected approach to obtain the apparent efficiency measured in a gas stand.

$$T_{4t}^{MFR_x} = T_4^{MFR_x} + \frac{c_4^2}{2c_p} \tag{35}$$

$$\begin{aligned}\eta_{MFR_x\ (t/s)}^{Sh_x/LV_x} = MFR_x \cdot \eta_{Sh_x/LV_x}^{TE/DV} + \frac{1 - MFR_x}{\left(1 - \left(\Pi_{0t,4}^{Sh_x/LV_x}\right)^{\frac{1-\gamma}{\gamma}}\right)} \\ \cdot \left[1 + \left(\eta_{H_x/SV_x}^{TE/DV}\left(1 - \left(\Pi_{0t,4}^{H_x/SV_x}\right)^{\frac{1-\gamma}{\gamma}}\right) - 1\right)\frac{T_{0t}^{H_x/SV_x}}{T_{0t}^{Sh_x/LV_x}}\right]\end{aligned} \tag{36}$$

$$\eta^{H_x/SV_x}_{MFR_x\ (t/s)} = (1 - MFR_x) \cdot \eta^{TE/DV}_{H_x/SV_x} + \frac{MFR_x}{\left(1 - \left(\Pi^{H_x/SV_x}_{0t,4}\right)^{\frac{1-\gamma}{\gamma}}\right)} \cdot \left[1 + \left(\eta^{TE/DV}_{Sh_x/LV_x}\left(1 - \left(\Pi^{Sh_x/LV_x}_{0t,4}\right)^{\frac{1-\gamma}{\gamma}}\right) - 1\right)\frac{T^{Sh_x/LV_x}_{0t}}{T^{H_x/SV_x}_{0t}}\right] \tag{37}$$

If both branches have the same temperature at the inlet (as could be the case in some gas-stand tests), Equations (36) and (37) are significantly simplified and Equations (38) and (39) are obtained.

$$\eta^{Sh_x/LV_x}_{MFR_x\ (t/s)} = MFR_x \cdot \eta^{TE/DV}_{Sh_x/LV_x} + (1 - MFR_x) \cdot \eta^{TE/DV}_{H_x/SV_x} \cdot \frac{\left(1 - \left(\Pi^{H_x/SV_x}_{0t,4}\right)^{\frac{1-\gamma}{\gamma}}\right)}{\left(1 - \left(\Pi^{Sh_x/LV_x}_{0t,4}\right)^{\frac{1-\gamma}{\gamma}}\right)} \tag{38}$$

$$\eta^{H_x/SV_x}_{MFR_x\ (t/s)} = (1 - MFR_x) \cdot \eta^{TE/DV}_{H_x/SV_x} + MFR_x \cdot \eta^{TE/DV}_{Sh_x/LV_x} \cdot \frac{\left(1 - \left(\Pi^{Sh_x/LV_x}_{0t,4}\right)^{\frac{1-\gamma}{\gamma}}\right)}{\left(1 - \left(\Pi^{H_x/SV_x}_{0t,4}\right)^{\frac{1-\gamma}{\gamma}}\right)} \tag{39}$$

$\eta^{TE/DV}_{Sh_x/LV_x}$ and $\eta^{TE/DV}_{H_x/SV_x}$ are the actual apparent efficiencies of individual branches that come from Equation (22) with the new z^j_i fitting function (Equation (34)) inside the $K^\star_2$ term. However, the merit function for fitting the coefficients are based on apparent efficiencies (Equations (36) and (37)) since they are what can be experimentally obtained. The z'^j coefficients are the same for the actual apparent efficiencies of two branches ($\eta^{TE/DV}_{Sh_x/LV_x}$ and $\eta^{TE/DV}_{H_x/SV_x}$) as the mixed turbine outlet temperature is common for both apparent efficiency definitions as expressed beforehand. In summary, both apparent efficiency equations (Equations (36) and (37)) have 11 fitting coefficients together and they are globally fitted using a non-linear fitting procedure for a given double entry turbine using the whole data points from the maps of the two branches (all available *MFR*s). For initial values, the fitting constants of mixed turbine outlet temperature model shown in Table 5 were used. A statistically based function, as shown in Equation (40), is used for minimizing the overall root mean square error of the apparent efficiencies of both branches, and also not to have very different errors between them.

$$\varepsilon_{RMS_{\text{overall}}} = \left(\varepsilon_{RMS_{\eta_{Shx}}} + \varepsilon_{RMS_{\eta_{Hx}}}\right) + \left|\varepsilon_{RMS_{\eta_{Shx}}} - \varepsilon_{RMS_{\eta_{Hx}}}\right| \tag{40}$$

In Figure 24a, the level of correlation between the experimental and modeled apparent efficiency values (Equations (36) and (37)) of twin-entry turbocharger is shown. It can be observed that modeled efficiency values of Shroud and Hub branch are well predicted with the experimental data, which is evidenced by the overall RMSE and individual branch RMSE values. It is worth highlighting that all the partial, unequal, and full admission flow efficiency values of each branch are well fitted at the same time and with the 11 fitting coefficients shown in Table 6. The final efficiency equations have been applied to the dual-volute turbine to validate the method outlined above. Figure 24b shows the agreement between the measured and predicted efficiency for long and short volute of the dual-volute turbine using Equations (36) and (37). This plot shows partial, unequal, and full admission flow data points taken for all different speed lines of both turbine inlets; however, all the values shown in Figure 24b have been normalized again by the peak efficiency point of each volute. The overall RMSE for the prediction of apparent efficiencies of two volutes is 0.0338 (i.e., around 3.4% mean error from normalized values). The model is able to capture all the apparent efficiency values of two branches at

different *MFR*s, and, by fitting with less number of *MFR* maps (only five *MFR*s in the case of T#2DV), it is also able to produce good results.

The results presented in Figure 24 were obtained by also using the reduced mass flow model previously described, since the efficiency model is mass flow oriented, i.e., using the model outlined above with 11 fitting parameters for the efficiency and 14 parameters for the reduced flow. As they are in different models, the number of measured points needed for fitting both models is not the addition of all of them but the higher number, i.e., 14. Therefore, at least 14 points, measured at three different *MFR*s (0, 1, and 0.5), are needed for a global model fitting of the whole double entry turbine.

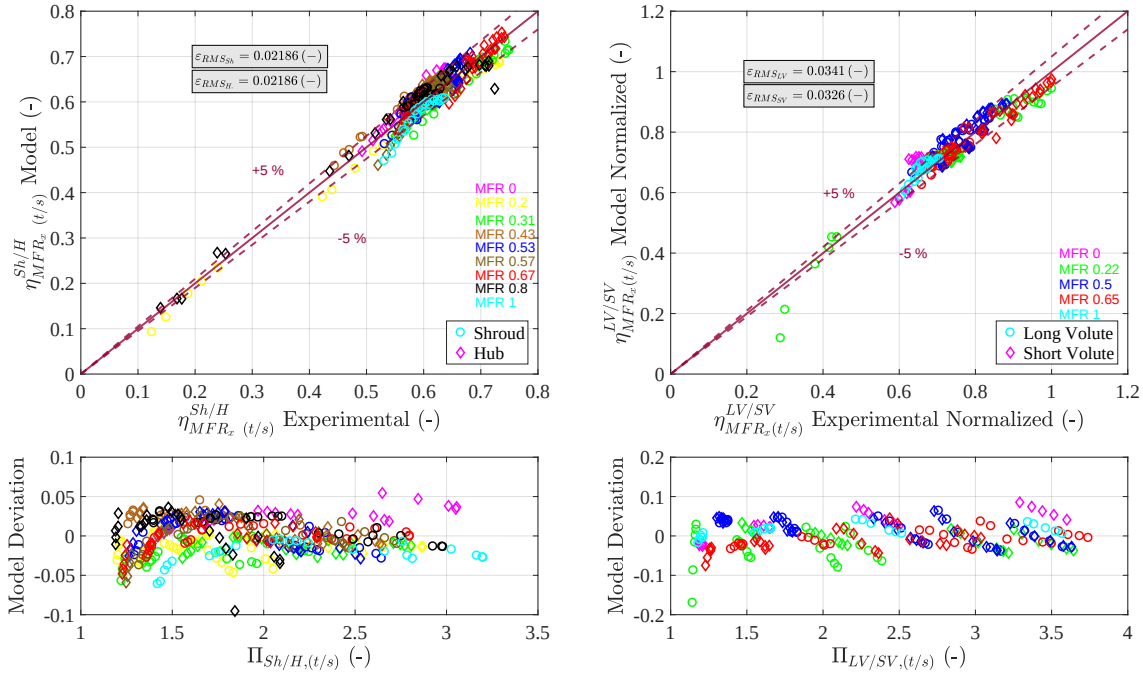

(**a**) Twin-entry (TE) turbocharger (T#1TE) (**b**) Dual-volute (DV) turbocharger (T#2DV)

Figure 24. Turbine apparent efficiency Modeled versus Experimental for both T#1TE and T#2DV turbochargers. Model constants are found using all the *MFR* data points of both branches together for that particular turbocharger.

The values of the coefficients of apparent efficiency model of both double entry turbines are summarized in Table 6, where MFR_1 and MFR_0 coefficients are applicable only for fitting the partial admission flows (i.e., having the flow only Shroud or Hub branch) and z' function coefficients act as a correction factor to increase the efficiency when the model goes from partial admission flows to full admission flows. From these results, it can be concluded that the apparent efficiency model developed here can be used for both types of double entry turbines and it is not necessary to modify the fitting equations. Moreover, the coefficient values are similar for twin-entry and dual-volute turbines. Thus, a different calibration is not necessary, and their average values can be used as initial values for fitting either twin or dual-volute turbine. While fitting the apparent efficiency model, it is also essential to take into consideration the geometry simplifications for this type of turbines, as explained in Section 3.

Table 6. Final apparent efficiency fitting coefficients for both T#1TE and T#2DV turbochargers. Model constants for both turbines are found in a global fitting using both branches together and all the *MFR*s data points.

Turbine Type	MFR_1			Fitting Function (z')					MFR_0		
	$b'_{Sh/LV}$	$c'_{Sh/LV}$	$f'_{Sh/LV}$	$k_0^{TE/DV}$	$k_1^{TE/DV}$	$k_2^{TE/DV}$	$k_3^{TE/DV}$	$k_4^{TE/DV}$	$b'_{H/SV}$	$c'_{H/SV}$	$f'_{H/SV}$
twin-entry	1.4471	0.1517	0.5767	4.0841	0.0753	0.2193	0.0582	6.721E-03	1.4164	0.1250	0.6643
dual-volute	1.3997	0.1041	0.9309	4.0735	0.0779	0.1862	0.0241	2.568E-03	1.4074	0.1354	0.9088

Table 7 shows the values of correlation quality for both double entry turbines studied in these papers, which is calculated using Equation (41) [47]. It is done to evaluate the predictive potential of the reduced mass flow and apparent efficiency models with there number of fitting coefficients.

$$R^2_{adj} = 1 - \frac{(n-1)\sum_{m=1}^{n}\left(V(m)_{\text{exp}} - V(m)_{\text{pred}}\right)^2}{(n-c)\sum_{m=1}^{n}\left(V(m)_{\text{exp}} - V(m)_{\text{mean}}\right)^2} \tag{41}$$

where V_{exp}, V_{pred}, and V_{mean} are the experimental, predicted, and mean experimental values, respectively. n is the number of data points and c is the number of fitting coefficients in the model. From the R^2_{adj} values shown in Table 7, it can be concluded that both models are well predicting the measured data, as the adjusted coefficient of determination values are closer to unity.

Table 7. Values of adjusted coefficient determination for both T#1TE and T#2DV.

Model	R Squred Adjusted R^2_{adj}			
	Twin-Entry		Dual-Volute	
	Shroud Branch	Hub Branch	Long Volute	Short Volute
Reduced mass flow	0.9963	0.9964	0.9952	0.9984
Apparent efficiency	0.9333	0.9287	0.9572	0.9319

6. Extrapolating Turbine Performance Parameters

The method for extrapolating the turbine performance parameters of the double entry turbines is based on the models developed in Sections 3 and 5. Both turbine branches should be extrapolated simultaneously since the apparent efficiency model of each turbine branch shown in Equations (36) and (37) are dependent on the expansion ratios, efficiency, and total inlet temperature between there turbine inlet branches. Besides, the reduced mass flow and apparent efficiency equations of each turbine inlet branch are interrelated. As the apparent efficiency (Equations (36) and (37)) appears in the reduced mass flow (Equation (18)), and the effective equivalent nozzle area (Equation (8)) which comes from the reduced mass flow appears in the apparent efficiency equations. Therefore, a system with the reduced mass flow and the apparent efficiency equations of both turbine branches should be solved together using an iterative procedure for the extrapolation purpose.

In Figure 25, the procedure used for extrapolating the performance maps of double entry turbine is presented. Following the flowchart, the extrapolation procedure starts with the input of the available map data of each turbine branch. By using this information, the equivalent nozzle area of each turbine branch can be solved from Equation (8) with the non-linear fitting procedure for finding the appropriate coefficient values ("*a*", "*b*", "*c*" and "*d*") of each turbine branch. Later, using the fitted "*d*" value, the next step will be estimating rotor inlet flow angle with the help of turbine geometry and also data from the maps. Later, using the information of efficiency maps of each turbine branch, the apparent efficiencies (Equations (36) and (37)) are fitted together to find the 11 fitting parameters that are discussed in Section 5. After obtaining all the necessary coefficients for the model, the system made of

Equations (8), (36) and (37) can be solved with an iterative procedure to obtain the extrapolated values of equivalent nozzle area and apparent efficiencies of each turbine branch. Finally, by substituting the extrapolated equivalent nozzle area values in Equation (18), the extrapolated reduced mass flow parameters can be obtained.

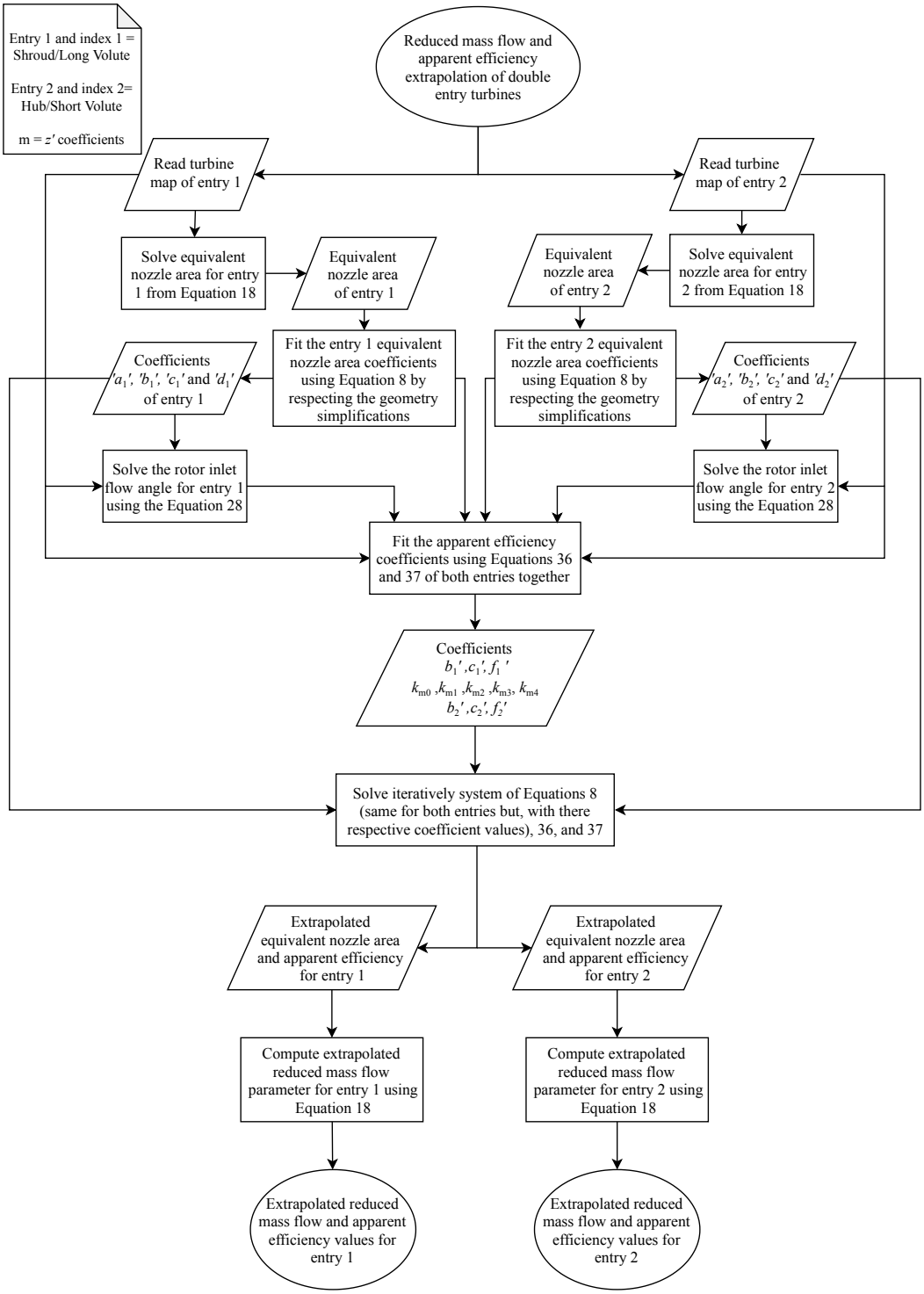

Figure 25. Procedure for extrapolating the reduced mass flow and apparent efficiency of double entry turbine.

6.1. Twin-Entry Turbine Extrapolation

For the extrapolation of reduced mass flow parameters, the coefficients in Table 2, which are graphically shown in Figure 12, are used. In the case of apparent efficiency, the fitting coefficients shown in Table 6 are used.

Figure 26 shows the model extrapolation results against experimental data for both reduced mass flow and apparent efficiency of T#1TE in Shroud and Hub branches. In Figure 26, the results of some *MFR*s are disclosed, including the unequal, full, and partial admission flows in the turbine. In Figure 26, it is clear that the extrapolation produced by the model (solid lines) at both lower and higher turbine reduced speeds in all the shown *MFR*s are not only in considerable accordance with the experimental data (different symbol points) for both branches but producing expected and consistent results. Figure 26a,b, shows the extrapolation results of reduced mass flow parameters in shroud and hub branch. In the shroud branch, it is notable that there is a small difference between the mass flow parameters at different reduced speeds for a given pressure ratio. This is due to the lower rotor inlet to outlet radius ratio in this branch (see Figure 9); therefore, it acts more like a low trimmed radial inflow turbine. However, this is not the case in hub branch (Figure 26b) due to the higher rotor inlet to outlet radius ratio.

The Figure 26c shows the extrapolation results of *MFR* 0.2 where the flow conditions are lower in shroud entry and model able to produce good accordance with the experimental data. However, it is notable that there are some errors found between the extrapolated and measured data at higher reduced speeds. It is worth highlighting that when the shroud branch is working at *MFR* 0.2, most of the flow expansion is produced by the hub branch and not by shroud one. Therefore, the actual efficiency of this branch should be much lower than the shown apparent efficiency, since it is getting the benefit of the lower mixed outlet temperature generated by the higher expansion in the vicinity branch. Similar results can be found in Figure 26d when the turbine is working at *MFR* 0.8. In this case, there is more flow in the shroud branch than hub branch.

Figure 26e,f shows the extrapolation result of unequal admission conditions, where the hub branch is having more flow than the shroud one. In this case, the model is also able to produce with good precision in both limbs at all speeds. Figure 26g,h shows extrapolation result when the turbine is working at almost full admission conditions. The model is able to predict well the peak efficiencies points for both branches. From the experimental data analysis, it was concluded that the maximum apparent efficiencies are always found when there is more flow in the hub side [12]. The extrapolation results from the model also show the same effect, i.e., the peak efficiencies of different reduced speeds can be seen with the higher flows in the Hub branch. Moreover, the extrapolation of having the flows only in Shroud or Hub are well captured by the model, as can be seen in Figure 26i,j. The overall quality of the prediction is high and both the reduced mass flow and apparent efficiency models can bring reasonable extrapolation in all the turbine reduced speeds in both branches.

6.2. Dual-Volute Turbine Extrapolation

Figure 27 shows the extrapolation results of reduced mass flow against the expansion ratio and apparent efficiency against the blade to jet speed ratio for both long and short volute entry. The results are presented for certain *MFR*s, including the partial, full, and unequal admission flow states. For this turbine, some exceptions were made to check the model capabilities in the extrapolations. In Figure 27, the filled points correspond to the data used for fitting the model and non-filled points correspond to the data used for checking the model predictions. In this way, the model has to extrapolate in the blade to jet speed ratios, reduced mass flows, and speeds in both turbine volutes. Figure 27a,c,e shows the results of long volute at mass flow ratios of 0.22 and 0.5; in these cases, the turbine reduced speed of 10,059 rpm/$\sqrt{\text{K}}$ has been fully extrapolated by the model for both reduced mass flow and apparent efficiencies of that volute.

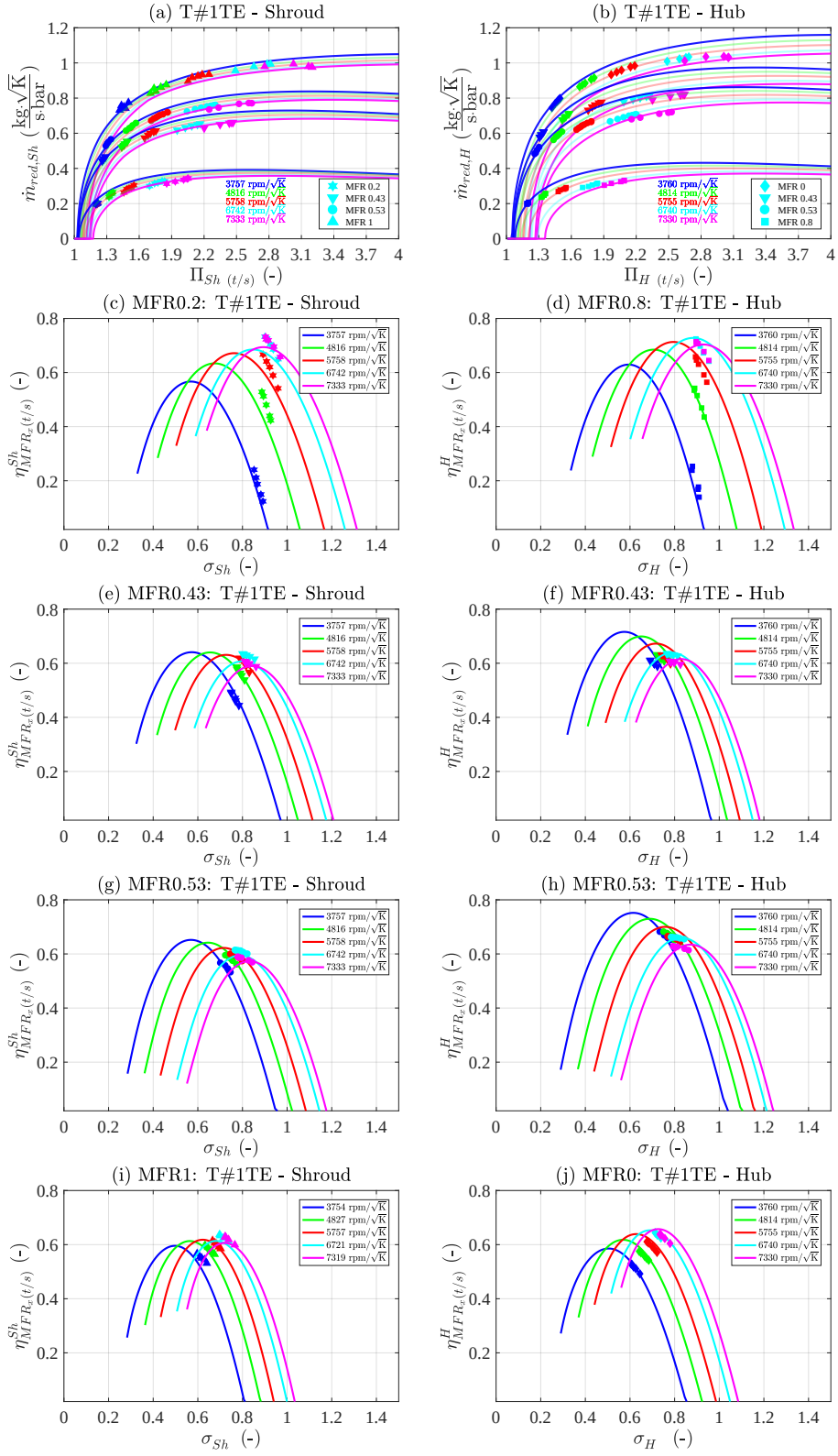

Figure 26. Reduced mass flow and apparent efficiency extrapolation to non-measured data points for Shroud and Hub branches of the twin-entry turbine using all maps fitting coefficients.

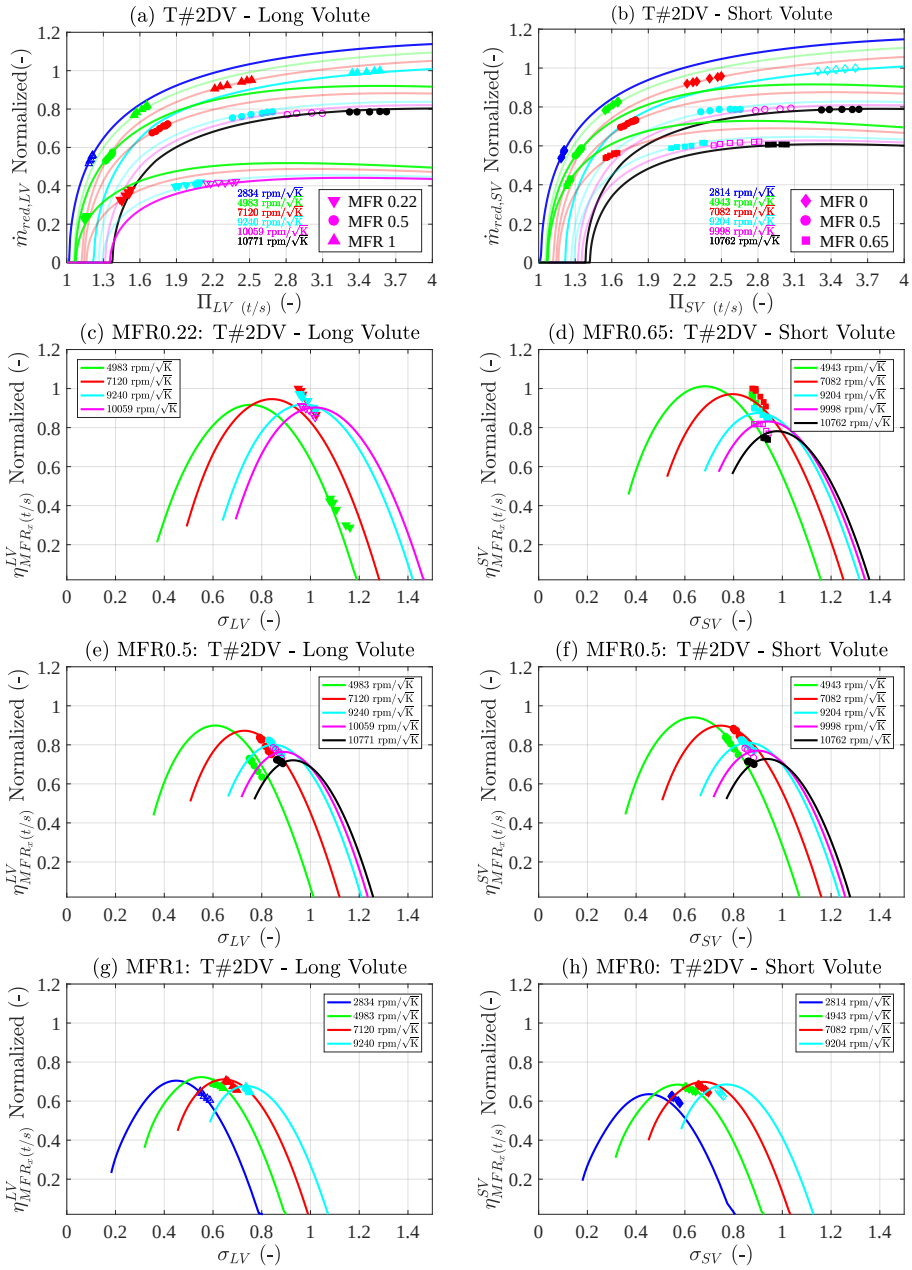

Figure 27. Dual-volute turbine reduced mass flow and apparent efficiency extrapolation for both volutes using only the filled points fitting coefficients. Non-filled points are predicted by the model.

Furthermore, in the case of *MFR* 1 in the long volute, the reduced speed of 2834 rpm/$\sqrt{\text{K}}$ has been extrapolated by the model and shows perfect accord with the experimental data. The same analysis was done with the short volute for the shown *MFR*s in Figure 27b,d,f and the outcomes from the model were quite aligned with the measurement data. In the case of extreme flow in short volute (*MFR* 0), the reduced speed of 9024 rpm/$\sqrt{\text{K}}$ extrapolated by the model shows notable differences compared to the experimental data.

The difference between the model and experimental data are maximum in the case of *MFR* 0.22 in the long volute at higher reduced speeds. This condition is where the flow is lower in that volute, and the short volute does most of the flow expansion. Some inconsistency is also seen at lower reduced speeds of *MFR*0.65 in short volute. Nevertheless, the model can extrapolate mass flow and efficiencies of both volutes considerable well in all the flow admission conditions.

7. Conclusions

In this paper, a model for extrapolating the performance maps of twin-entry and dual-volute radial inflow turbines in terms of different flow admission conditions, rotational speed, and blade to jet speeds ratios is presented. For the development of the model, both double entry turbines were tested at different flow admission conditions in a special turbocharger gas stand. The procedure for analyzing the performance maps of this type of turbines is outlined in this paper, and the detailed discussions are presented in [12]. Systematizing the performance maps of double entry turbines gave the awareness to model any double entry turbine as if it is formed of two VGTs and made it possible to extrapolate the maps to off-design conditions.

For extrapolating the reduced mass flow parameter of double entry turbines, the method uses seven calibration coefficients for each branch, which are fitted using the available turbine map dataset. Seven coefficients are fitted independently using the turbine map corresponding to Entry 1, and the other seven are adjusted using the turbine map corresponding to Entry 2. The reduced mass flow coefficients must be fitted first since one of them is used for estimating the rotor flow inlet angle of each turbine branch and they are used in the efficiency model equation.

Due to the assumption of each turbine inlet being an individual turbine, their apparent efficiencies are computed using the respective branch turbine inlet temperature and mixed temperature available at the outlet of the turbine. Therefore, to take into account these mixing effects in the efficiency model, the based VGT efficiency model has been refined by analyzing the twin-entry turbocharger experimental data. Eventually, a new corrected mixed flow efficiency model has been developed in this paper, and that model uses 11 calibration coefficients to fit the efficiencies of both turbine branches. The model is also validated using the dual-volute turbine data of each volute and the results are in accordance with the experimental information. It is also essential to take into account the geometrical simplifications of different double entry turbines demonstrated in this paper while fitting both reduced mass flow and apparent efficiency models.

After fitting the calibration coefficients of a double entry turbine, for extrapolation purposes, a system with the reduced mass flow and apparent efficiency of both individual turbine branches must be solved together, using an iterative procedure, as the mass flow and apparent efficiency variables of each branch are interconnected. The extrapolation results show good agreement with the experimental data for both twin-entry and dual-volute turbines. From the results, it can be concluded that both reduced mass flow and apparent efficiency models can extrapolate beyond normal turbine map measured range in whatever mass flow ratios, reduced turbine speed, and blade to jet speed ratio for each turbine branch.

One of the main advantages of the model is that it can be used for both twin-entry and dual-volute turbines just by giving attention to the geometrical simplifications while fitting the type of turbine. It is essential to have a standard turbine map of each turbine branch measured in nearly adiabatic conditions and with at least two extreme flow conditions (one in each turbine branch (*MFR* 0 and 1)) and also one full admission flow state (where the flow is equally shared in between the entries of the turbine). These three flow admission conditions are needed to fit the coefficients of reduced mass flow and apparent efficiency model and also for extrapolating to other *MFR*s. However, the more information there is on the flow conditions in each turbine branch, the better is the performance of the extrapolation capabilities of the model.

Author Contributions: J.R.S., L.M.G.-C., F.J.A. and V.S. proposed the idea, conceptualization and performed data analysis; V.S. performed experimentation and modelling work under the supervision of J.R.S., L.M.G.-C. and F.J.A.; V.S. and J.R.S. prepared the original draft. Further, all authors have contributed in the revision and organization of the paper. All authors have read and agreed to the published version of the manuscript.

Funding: Vishnu Samala is partially supported through contract FPI-2017-S2-1256 of Programa de Apoyo para la Investigación y Desarrollo (PAID) of Universitat Politècnica de València. This work was partially funded by the 'Ayuda a Primeros Proyectos de Investigación' (PAID-06-18), Vicerrectorado de Investigación, Innovación y Transferencia de la Universitat Politècnica de Valéncia (UPV), València, Spain.

Acknowledgments: The authors wish to thank M.A. Ortiz and R. Carrascosa for their invaluable work during the experimental setup and campaign.

Conflicts of Interest: The authors declare no conflict of interest.

Nomenclature

A	Area (m)
a	Rotor discharge coefficient (-)
a'	Apparent efficiency fitting coefficient (-)
Bh	Blade height (m)
b	Reduced mass flow fitting coefficient (-)
b'	Apparent efficiency fitting coefficient (-)
BEVs	Battery Electric Vehicles (-)
BSR	Blade Speed Ratio (-)
c'	Apparent efficiency fitting coefficient (-)
c	Reduced mass flow fitting coefficient (-)
c_p	Specific heat capacity (J kg^{-1} K^{-1})
C_D	Discharge coefficient (-)
C_{ss}	Isentropic jet velocity (ms^{-1})
d'	Apparent efficiency fitting coefficient (-)
D	Diameter (m)
DV	Dual-volute (-)
e'	Apparent efficiency fitting coefficient (-)
EGR	Exhaust Gas Recirculation (-)
ETE	Effective Turbine Efficiency (-)
f'	Apparent efficiency fitting coefficient (-)
ILS	Independent Lubrication System (-)
H	Hub (-)
K	Efficiency equation coefficient (-)
k_0	Apparent efficiency fitting coefficient (-)
k_1	Apparent efficiency fitting coefficient (-)
k_2	Apparent efficiency fitting coefficient (-)
k_3	Apparent efficiency fitting coefficient (-)
k_4	Apparent efficiency fitting coefficient (-)
LV	Long Volute (-)
$\dot{m}$	Mass flow (kg/s)
MFR	Mass Flow Ratio (-)
n	Rotational speed (rpm)
p	Pressure (Pa)
r	Rotor radius (m)
Sh	Shroud (-)
SV	Short Volute (-)
T	Temperature (K)
TE	Twin-entry (-)
u	Blade tip speed (ms^{-1})
v	Absolute velocity (ms^{-1})
VGT	Variable Geometry Turbine (-)
VNT	Variable Nozzle Turbine (-)
$\Delta h_{MFR_x}^{Sh/LV}$	Apparent work Entry 1
$\Delta h_{MFR_x}^{H/SV}$	Apparent work Entry 2
$\Delta h_{Sh_x/LV_x}$	Actual work Entry 1
$\Delta h_{H_x/SV_x}$	Actual work Entry 2
$\Delta h_{S,Sh_x/LV_x}$	Isentropic work Entry 1
$\Delta h_{S,H_x/SV_x}$	Isentropic work Entry 2

Subscripts and Superscript

0	Turbine inlet static states
0t	Turbine inlet total states
4	Turbine outlet static states
4s	Turbine isentropic state
4t	Turbine outlet total states
4m	Average value at the rotor outlet
eff	Refers to effective equivalent nozzle
exp	Experimental value
flow	Refers to the flow
geom	Refers to geometry
i	Discriminates Sh from H in TE or LV from SV in DV
j	Refers to TE or to DV turbine
mean	Mean value
pred	Predicted value
red	Refers to reduced variables
r	Radial
Neq	Refers to equivalent nozzle
t/s	Total to static

Greek letters

Π	Corresponding pressure ratio
η	Corresponding efficiency
γ	Heat capacity ratio
σ	Corresponding blade speed ratio
α	Absolute velocity angle (rad)
β	Relative velocity angle (rad)

Appendix A. Description of VGT Flow Oriented Model

Appendix A.1. Mass Flow Model

The procedure developed by the authors of [30,43] for modeling the turbine mass flow parameter is mainly based on viewing the turbine as a single equivalent nozzle that covers from station 0 to 4 of the radial turbine, as shown in Figure A1. The primary assumption of this model is the behavior of the turbine is quasi-steady throughout the nozzle simulating the turbine; from both the thermodynamic and fluid dynamics perspective. The fundamental approach followed by Serrano et al. [30] is calculating for every turbine operating point an equivalent nozzle flow area (A_{eff}) that represents the whole turbine expansion. Accordingly, this equivalent nozzle flow area (A_{eff}) should allow calculating the mass flow parameter for the entire operative range of the turbine; thus, it is possible to plot the whole mass flow curve. To do so, first, the continuity equation is applied to stator, rotor and equivalent nozzle, as shown in Equation (A1). Then, using the velocity definition and solving the mass flow, an expression for the equivalent nozzle area shown in Equation (A2) is obtained. By assuming a certain hypothesis, as described in the work of Serrano et al. [30], and doing some simplifications, a new expression of the throat area of the equivalent nozzle is obtained, as shown in Equation (A3). It mainly depends on the information available in a standard turbocharger map and the measurable geometry of the turbine with four fitting constants (a, b, c, and d) in Equation (A3).

$$\dot{m} = A_{2'}\rho_{2'}v_{2'} = A_4\rho_4 v_4 = A_{Neq}\rho_4 v_{Neq} \tag{A1}$$

$$A_{Neq} = A_4\sqrt{\frac{1+\left(\frac{u_4}{v_{Neq}}\right)^2-\left(\frac{u_3}{v_{Neq}}\right)^2+\left(\frac{w_3}{v_{Neq}}\right)^2}{\left(\frac{A_4}{A_{2'}}\right)^2\left(\frac{\rho_4}{\rho_{2'}}\right)^2+1}} \tag{A2}$$

$$A_{\text{eff}} = \frac{a \cdot A_4^{\text{geom}} \cdot \sqrt{1 + \frac{\sigma^2 \left[\left(\frac{D_{4m}}{D_3} \right)^2 - 1 \right] + b}{\overline{\eta}_{ts}}}}{\sqrt{1 + \left(c \cdot \frac{A_4^{\text{geom}}}{A_{2'}^{\text{geom}}} \right)^2 \cdot \frac{\left(\frac{1}{\Pi_{2',4}} \right)^2}{\left(1 - \eta_{ts} \cdot \left(1 - \left(\frac{1}{\Pi_{2',4}} \right)^{\frac{\gamma-1}{\gamma}} \right) \right)^2}}} \tag{A3}$$

where $A_{2'}^{\text{geom}}$ is the geometrical throat section of the stator vanes and can be calculated for any VGT as described in [30]. The rotor outlet geometrical area (A_4^{geom}) is calculated by taking the arithmetic diameter between the turbine rotor shroud (D_4) and rotor hub (D_{nut}) diameters, as shown in Equation (A4).

$$A_4^{\text{geom}} = \pi \cdot \left(\frac{D_4^2 - D_{nut}^2}{4} \right) \tag{A4}$$

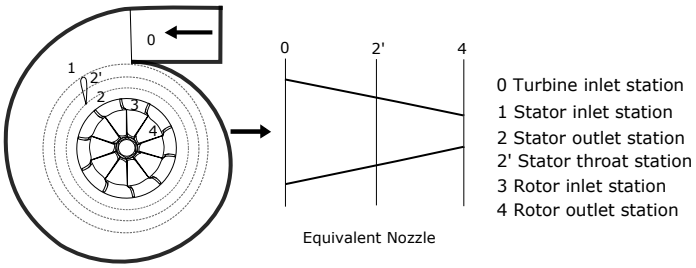

Figure A1. Turbine as single equivalent nozzle and stations distribution.

In Equation (A3), D_3 is turbine rotor diameter, D_{4m} is the mean diameter between turbine rotor shroud (D_4) and rotor hub (D_{nut}) diameters, η_{ts} represents the turbine total-static adiabatic efficiency, σ is the blade to jet speed ratio calculated using the Equation (A5), and $\Pi_{2',4}$ represents pressure ratio in the VGT rotor. $\Pi_{2',4}$ is calculated from the total to static turbine pressure ratio by using a fitting constant "d" as shown in Equation (A6). It is obtained by making the hypothesis that the turbine stator pressure drop to the whole turbine total-to-static pressure drop ratio is constant for a VGT position [30]. A constant average value of turbine efficiency ($\eta_{ts} = \overline{\eta}_{ts} = 0.8$) is assumed relaying on "b" coefficient to avoid the possible inconsistency during the extrapolations.

$$\sigma = \frac{2 \cdot \pi \cdot n \cdot r_3}{\sqrt{2 \cdot c_p \cdot T_{0t} \cdot \left[1 - \left(\frac{1}{\Pi_{0t,4}} \right)^{\frac{\gamma-1}{\gamma}} \right]}} \tag{A5}$$

$$\Pi_{2',4} = 1 + d \cdot (\Pi_{0t,4} - 1) \tag{A6}$$

The coefficients "a" and "c" in Equation (A3) are directly related to the rotor and stator discharge coefficient. The other two coefficients ("b" and "d") come from the theoretical considerations previously described (more details can be read in [30]). These four fitting parameters are calculated using regression analysis, with the help of a suppliers performance map and the turbocharger geometry data as input to the model. Once the equivalent nozzle (Equation (A3)) is known for every turbine operative point, the reduced mass flow parameter can be calculated using the definition of the sub-critical mass flow parameter through an orifice of single isentropic nozzle given by Equation (A7).

$$\dot{m}_{\text{red}} = A_{\text{eff}} \cdot \sqrt{\frac{\gamma}{R}} \cdot \left(\frac{1}{\Pi_{0t,4}} \right)^{\frac{1}{\gamma}} \cdot \sqrt{\frac{2}{\gamma - 1} \cdot \left[1 - \left(\frac{1}{\Pi_{0t,4}} \right)^{\frac{\gamma-1}{\gamma}} \right]} \tag{A7}$$

Appendix A.2. Efficiency Model

The efficiency model presented in [30] is based on the use of the Euler equation of turbo-machinery for radial gas turbines and assuming constant meridional component velocities. By this, both assumptions, and doing some simplifications, the definition of the total to static adiabatic efficiency of the turbine (Equation (A8)) can be expressed as Equation (A9).

$$\eta_{t/s} = \frac{T_{0t} - T_{4t}}{T_{0t} - T_{4ts}} \tag{A8}$$

$$\eta_{t/s} = \frac{u_3 c_0 \, tan\, \alpha_3 - \left[u_3 \left(\frac{r_4}{r_3}\right) - c_0 \, tan\, \beta_4\right] u_3 \left(\frac{r_4}{r_3}\right)}{c_p T_{0t} \left(1 - \left(\frac{1}{\Pi_{0t,4}}\right)^{\frac{\gamma-1}{\gamma}}\right)} \tag{A9}$$

Based on the definition of blade to jet speed ratio (σ) in Equation (A5), Equation (A10) is obtained for a constant tip speed maps.

$$\eta_{t/s} = -2 \cdot \left(\frac{r_4}{r_3}\right)^2 \cdot \sigma^2 + 2 \cdot \frac{A_{\text{eff}}}{A_0^{\text{geom}}} \cdot \left(tan\, \alpha_3 + \frac{r_4}{r_3} \cdot tan\, \beta_4\right) \left[\frac{1}{\Pi_{0t,4}}\right]^{\frac{1}{\gamma}} \cdot \sigma \tag{A10}$$

It is worth highlighting that the above equation is dependent on A_{eff}, which can be calculated using Equation (A3). The rotor inlet flow angle (α_3) is estimated as a function of stator outlet flow angle (φ_2^{metal}), as shown in Equation (A11) [13,30]

$$tan\, \alpha_3 = z_3^{\text{geom}} \cdot sin\, \varphi_2^{metal} \tag{A11}$$

Coefficient z_3^{geom} is based on the geometry of VGT stator vanes and was obtained theoretically, as described in [30]. The final turbine efficiency equation is lumped into K_i terms, as shown in Equation (A12). A fitting parameter "z" is introduced into $K_2^\star$ and it has six coefficients that mainly depend on the reduced turbine speed, blade to jet speed ratio, and VGT position, as shown in Equation (A15). Equations (A13) and (A16) are related to physical values from the turbine geometry and turbine map, as described in [30].

$$\eta_{t/s} = -K_1 \cdot \sigma^2 + K_2^\star \cdot \left(1 - \frac{K_3}{\sigma^2}\right)^{\frac{1}{\gamma-1}} \cdot \sigma \tag{A12}$$

$$K_1 = 2\left(\frac{r_4}{r_3}\right)^2 \tag{A13}$$

$$K_2^\star = 2\frac{A_{\text{eff}}}{A_0^{\text{geom}}} \left(z \cdot z_3^{\text{geom}} sin(\varphi_2^{metal}) + \sqrt{\frac{K_1}{2}} tan(\beta_4^{metal})\right) \tag{A14}$$

$$z = -(a' \cdot n_{\text{red}} + b') \cdot \sigma + (c' \cdot n_{\text{red}} + d' \cdot VGT^2 + e' \cdot VGT + f') \tag{A15}$$

$$K_3 = \frac{u_{3,red}^2}{2c_p} \tag{A16}$$

References

1. Haq, G.; Weiss, M. CO2 labelling of passenger cars in Europe: Status, challenges, and future prospects. *Energy Policy* **2016**, *95*, 324–335. doi:10.1016/j.enpol.2016.04.043.
2. Wang, S.; Zhao, F.; Liu, Z.; Hao, H. Heuristic method for automakers' technological strategy making towards fuel economy regulations based on genetic algorithm: A China's case under corporate average fuel consumption regulation. *Appl. Energy* **2017**, *204*, 544–559. doi:10.1016/j.apenergy.2017.07.076.

3. Kalghatgi, G. Is it really the end of internal combustion engines and petroleum in transport? *Appl. Energy* **2018**, *225*, 965–974. doi:10.1016/j.apenergy.2018.05.076.
4. Romare, M.; Dahllöf, L. The Life Cycle Energy Consumption and Greenhouse Gas Emissions from Lithium-Ion Batteries. *IVL Swed. Environ. Res. Inst.* **2017**, 8–42. doi:978-91-88319-60-9.
5. Serrano, J.R. Imagining the Future of the Internal Combustion Engine for Ground Transport in the Current Context. *Appl. Sci.* **2017**, *7*, 1001. doi:10.3390/app7101001.
6. Heywood, J.; MacKenzie, D.; Akerlind, I.B.; Bastani, P.; Berry, I.; Bhatt, K.; Zoepf, S. *On the Road toward 2050: Potential for Substantial Reductions in Light-Duty Vehicle Energy Use and Greenhouse Gas Emissions*; Massachusetts Institute of Technology: Cambridge, MA, USA, 2015.
7. Kruiswyk, R. The role of turbocompound in the era of emissions reduction. In Proceedings of the 10th International Conference on Turbochargers and Turbocharging, London, UK, 29–30 May 2012; IMechE, Ed.; Woodhead Publishing: Sawston, UK, 2012; pp. 269–280. doi:10.1533/9780857096135.5.269.
8. Yang, M.; Deng, K.; Martines-Botas, R.; Zhuge, W. An investigation on unsteadiness of a mixed-flow turbine under pulsating conditions. *Energy Convers. Manag.* **2016**, *110*, 51–58. doi:10.1016/J.ENCONMAN.2015.12.007.
9. Zhu, D.; Zheng, X. Asymmetric twin-scroll turbocharging in diesel engines for energy and emission improvement. *Energy* **2017**, *141*, 702–714. doi:10.1016/j.energy.2017.07.173.
10. Pischinger, F.; Wunsche, A. The characteristic behaviour of radial turbines and its influence on the turbocharging process. In Proceedings of the CIMAC Conference, Tokyo, Japan, 23–27 May 1977.
11. Romagnoli, A.; Copeland, C.D.; Martinez-Botas, R.F.; Seiler, M.; Rajoo, S.; Costall, A. Comparison Between the Steady Performance of Double-Entry and Twin-Entry Turbocharger Turbines. *J. Turbomach.* **2012**, *135*. doi:10.1115/1.4006566.
12. Serrano, J.R.; Arnau, F.J.; García-Cuevas, L.M.; Samala, V.; Smith, L. Experimental approach for the characterization and performance analysis of twin entry radial-inflow turbines in a gas stand and with different flow admission conditions. *Appl. Therm. Eng.* **2019**, 113737. doi:10.1016/j.applthermaleng.2019.113737.
13. Watson, N.; Janota, M. *Turbocharging the Internal Combustion Engine*; Macmillan: New York, NY, USA, 1982. doi:10.1007/978-1-349-04024-7.
14. Cerdoun, M.; Ghenaiet, A. Characterization of a twin-entry radial turbine under pulsatile flow condition. *Int. J. Rotat. Mach.* **2016**. doi:10.1155/2016/4618298.
15. Winkler, N.; Ångström, H.E.; Olofsson, U. Instantaneous On-Engine Twin-Entry Turbine Efficiency Calculations on a Diesel Engine. In Proceedings of the Powertrain & Fluid Systems Conference & Exhibition, San Antonio, TX, USA, 24–27 October 2005; SAE International: Warrendale, PA, USA, 2005. doi:10.4271/2005-01-3887.
16. Fiaschi, D.; Lifshitz, A.; Manfrida, G.; Tempesti, D. An innovative ORC power plant layout for heat and power generation from medium- to low-temperature geothermal resources. *Energy Convers. Manag.* **2014**, *88*, 883–893. doi:10.1016/J.ENCONMAN.2014.08.058.
17. Zare, V. A comparative exergoeconomic analysis of different ORC configurations for binary geothermal power plants. *Energy Convers. Manag.* **2015**, *105*, 127–138. doi:10.1016/J.ENCONMAN.2015.07.073.
18. Daabo, A.M.; Al Jubori, A.; Mahmoud, S.; Al-Dadah, R.K. Parametric study of efficient small-scale axial and radial turbines for solar powered Brayton cycle application. *Energy Convers. Manag.* **2016**, *128*, 343–360. doi:10.1016/J.ENCONMAN.2016.09.060.
19. Cheng, Z.; Tong, S.; Tong, Z. Bi-directional nozzle control of multistage radial-inflow turbine for optimal part-load operation of compressed air energy storage. *Energy Convers. Manag.* **2019**, *181*, 485–500. doi:10.1016/J.ENCONMAN.2018.12.014.
20. Wei, D.; Lu, X.; Lu, Z.; Gu, J. Performance analysis and optimization of organic Rankine cycle (ORC) for waste heat recovery. *Energy Convers. Manag.* **2007**, *48*, 1113–1119. doi:10.1016/J.ENCONMAN.2006.10.020.
21. Cho, C.H.; Cho, S.Y.; Ahn, K.Y. A study of partial admission characteristics on a small-scale radial-inflow turbine. *Proc. Inst. Mech. Eng. Part A J. Power Energy* **2010**, *224*, 737–748. doi:10.1243/09576509JPE865.
22. Cho, S.Y.; Cho, C.H.; Ahn, K.Y.; Lee, Y.D. A study of the optimal operating conditions in the organic Rankine cycle using a turbo-expander for fluctuations of the available thermal energy. *Energy* **2014**, *64*, 900–911. doi:10.1016/j.energy.2013.11.013.

23. Shin, H.; Cho, J.; Baik, Y.J.; Cho, J.; Roh, C.; Ra, H.S.; Kang, Y.; Huh, J. Partial Admission, Axial Impulse Type Turbine Design and Partial Admission Radial Turbine Test for SCO2 Cycle, Volume 9: Oil and Gas Applications; Supercritical CO2 Power Cycles, Wind Energy. In Proceedings of the Turbo Expo: Power for Land, Sea, and Air, Charlotte, NC, USA, 26–30 June 2017; doi:10.1115/GT2017-64349.
24. Ding, Z.; Zhuge, W.; Zhang, Y.; Chen, H.; Martinez-Botas, R.; Yang, M. A one-dimensional unsteady performance model for turbocharger turbines. *Energy* **2017**, *132*, 341–355. doi:10.1016/j.energy.2017.04.154.
25. Martin, G.; Talon, V.; Higelin, P.; Charlet, A.; Caillol, C. Implementing Turbomachinery Physics into Data Map-Based Turbocharger Models. *SAE Int. J. Eng.* **2009**, *2*, 211–229. doi:10.4271/2009-01-0310.
26. Fang, X.; Dai, Q. Modeling of turbine mass flow rate performances using the Taylor expansion. *Appl. Therm. Eng.* **2010**, *30*, 1824–1831. doi:10.1016/j.applthermaleng.2010.04.016.
27. Romagnoli, A.; Martinez-Botas, R. Performance prediction of a nozzled and nozzleless mixed-flow turbine in steady conditions. *Int. J. Mech. Sci.* **2011**, *53*, 557–574. doi:10.1016/j.ijmecsci.2011.05.003.
28. Chiong, M.; Rajoo, S.; Romagnoli, A.; Costall, A.; Martinez-Botas, R. Integration of meanline and one-dimensional methods for prediction of pulsating performance of a turbocharger turbine. *Energy Convers. Manag.* **2014**, *81*, 270–281. doi:10.1016/j.enconman.2014.01.043.
29. Serrano, J.R.; Arnau, F.J.; Dolz, V.; Tiseira, A.; Cervelló, C. A model of turbocharger radial turbines appropriate to be used in zero- and one-dimensional gas dynamics codes for internal combustion engines modelling. *Energy Convers. Manag.* **2008**, *49*, 3729–3745. doi:10.1016/j.enconman.2008.06.031.
30. Serrano, J.R.; Arnau, F.J.; García-Cuevas, L.M.; Dombrovsky, A.; Tartoussi, H. Development and validation of a radial turbine efficiency and mass flow model at design and off-design conditions. *Energy Convers. Manag.* **2016**, *128*, 281–293. doi:10.1016/j.enconman.2016.09.032.
31. Serrano, J.R.; Arnau, F.J.; García-Cuevas, L.M.; Inhestern, L.B. An innovative losses model for efficiency map fitting of vaneless and variable vaned radial turbines extrapolating towards extreme off-design conditions. *Energy* **2019**. doi:10.1016/j.energy.2019.05.062.
32. Chiong, M.; Rajoo, S.; Martinez-Botas, R.; Costall, A. Engine turbocharger performance prediction: One-dimensional modeling of a twin entry turbine. *Energy Convers. Manage.* **2012**, *57*, 68–78. doi:10.1016/j.enconman.2011.12.001.
33. Hajilouy Benisi, A.; Rad, M.; Reza Shahhosseini, M. Modeling of Twin-Entry Radial Turbine Performance Characteristics Based on Experimental Investigation Under Full and Partial Admission Conditions. *Trans. B Mech. Eng.* **2009**, *16*, 281–290.
34. Costall, A.; Mcdavid, R.; Martinez-Botas, R.; C. Baines, N. Pulse Performance Modeling of a Twin Entry Turbocharger Turbine Under Full and Unequal Admission. *J. Turbomach.* **2011**, *133*, 021005–1. doi:10.1115/1.4000566.
35. Newton, P.; Romagnoli, A.; Martinez-Botas, R.; Copeland, C.; Seiler, M. A method of map extrapolation for unequal and partial admission in a double entry turbine. *J. Turbomach. Trans. ASME* **2013**, *136*. doi:10.1115/1.4025763.
36. Chiong, M.; Rajoo, S.; Romagnoli, A.; Costall, A.; Martinez-Botas, R. One-dimensional pulse-flow modeling of a twin-scroll turbine. *Energy* **2016**, *115*, 1291–1304. doi:10.1016/j.energy.2016.09.041.
37. Fredriksson, C.; Qiu, X.; Baines, N.; Müller, M.; Brinkert, N.; Gutmann, C. Meanline Modeling of Radial Inflow Turbine With Twin-Entry Scroll. In Proceedings of the ASME Turbo Expo 2012: Turbine Technical Conference and Exposition, Copenhagen, Denmark, 11–15 June 2012; Volume 5, pp. 713-720. doi:10.1115/GT2012-69018.
38. Macek, J.; Zak, Z.; Vitek, O. Physical Model of a Twin-scroll Turbine with Unsteady Flow. In *SAE 2015 World Congress and Exhibition*; SAE International: Warrendale, PA, USA, 2015. doi:10.4271/2015-01-1718.
39. Palenschat, T.; Mueller, M.; Rajoo, S.; Chiong, M.S.; Newton, P.; Martinez-Botas, R.; Tan, F.X. *Steady-State Experimental and Meanline Study of an Asymmetric Twin-Scroll Turbine at Full and Unequal and Partial Admission Conditions*; SAE Technical Paper; SAE International: Warrendale, PA, USA; 2018. doi:10.4271/2018-01-0971.
40. Brinkert, N.; Sumser, S.; Weber, S.; Fieweger, K.; Schulz, A.; Bauer, H.J. Understanding the Twin Scroll Turbine: Flow Similarity. *J. Turbomach.* **2012**, *135*. doi:10.1115/1.4006607.
41. Semlitsch, B.; Wang, Y.; Mihăescu, M. Flow effects due to valve and piston motion in an internal combustion engine exhaust port. *Energy Convers. Manag.* **2015**, *96*, 18–30. doi:10.1016/J.ENCONMAN.2015.02.058.
42. Serrano, J.R.; Tiseira, A.; García-Cuevas, L.M.; Inhestern, L.B.; Tartoussi, H. Radial turbine performance measurement under extreme off-design conditions. *Energy* **2017**, *125*, 72–84. doi:10.1016/j.energy.2017.02.118.

43. Payri, F.; Serrano, J.R.; Fajardo, P.; Reyes-Belmonte, M.A.; Gozalbo-Belles, R. A physically based methodology to extrapolate performance maps of radial turbines. *Energy Convers. Manag.* **2012**, *55*, 149–163. doi:10.1016/j.enconman.2011.11.003.
44. Xue, Y.; Yang, M.; Martinez-Botas, R.F.; Romagnoli, A.; Deng, K. Loss analysis of a mix-flow turbine with nozzled twin-entry volute at different admissions. *Energy* **2019**, *166*, 775–788. doi:10.1016/j.energy.2018.10.075.
45. Serrano, J.R.; Navarro, R.; García-Cuevas, L.M.; Inhestern, L. Turbocharger turbine rotor tip leakage loss and mass flow model valid up to extreme off-design conditions with high blade to jet speed ratio. *Energy* **2018**, *147*, 1299–1310. doi:10.1016/j.energy.2018.01.083.
46. Serrano, J.R.; Olmeda, P.; Arnau, F.J.; Samala, V. A holistic methodology to correct heat transfer and bearing friction losses from hot turbocharger maps in order to obtain adiabatic efficiency of the turbomachinery. *Int. J. Eng. Res.* **2019**, doi:10.1177/1468087419834194.
47. Harrell, F.E. Ordinal Logistic Regression. In *Regression Modeling Strategies: With Applications to Linear Models, Logistic Regression, and Survival Analysis*; Springer: New York, NY, USA, 2001; pp. 331–343. doi:10.1007/978-1-4757-3462-1_13.